Mitotic phosphorylation by NEK6 and NEK7 reduces microtubule affinity of EML4 to promote chromosome congression

Rozita Adib[1], Jessica M. Montgomery[1], Joseph Atherton[2], Laura O'Regan[1], Mark W. Richards[3], Kees R. Straatman[4], Daniel Roth[5], Anne Straube[5], Richard Bayliss[3], Carolyn A. Moores[2] and Andrew M. Fry[1,*]

[1]Department of Molecular and Cell Biology, University of Leicester, Lancaster Road, Leicester LE1 9HN, U.K.

[2]Institute of Structural and Molecular Biology, Birkbeck College, Malet Street, London WC1E 7HX, U.K.

[3]Astbury Centre for Structural Molecular Biology, Faculty of Biological Sciences, University of Leeds, Leeds LS2 9JT, U.K.

[4]Centre for Core Biotechnology Services, University of Leicester, University Road, Leicester, LE1 7RH, UK.

[5]Centre for Mechanochemical Cell Biology, Warwick Medical School, University of Warwick, Coventry CV4 7AL, U.K.

[*]Corresponding author.

Email: amf5@le.ac.uk

ABSTRACT

EML4 is a microtubule-associated protein that promotes microtubule stability. We investigated its regulation across the cell cycle and found that EML4 was distributed as punctate foci along the microtubule lattice in interphase but exhibited reduced association with spindle microtubules in mitosis. Microtubule sedimentation and cryo-electron microscopy with 3D reconstruction revealed that the basic N-terminal domain of EML4 mediated its binding to the acidic C-terminal tails of α- and β-tubulin on the microtubule surface. The mitotic kinases NEK6 and NEK7 phosphorylated the EML4 N-terminal domain at Ser^{144} and Ser^{146} in vitro, and depletion of these kinases in cells led to increased EML4 binding to microtubules in mitosis. An S144A-S146A double mutant not only bound inappropriately to mitotic microtubules but also increased their stability and interfered with chromosome congression. Meanwhile, constitutive activation of NEK6 or NEK7 reduced EML4 association with interphase microtubules. Together, these data support a model in which NEK6- and NEK7-dependent phosphorylation promotes dissociation of EML4 from microtubules in mitosis in a manner that is required for efficient chromosome congression.

INTRODUCTION

Dynamic instability is an essential property of microtubules that allows them to play diverse roles in intracellular trafficking, organelle positioning, cell migration and cell division (*1*). Furthermore, the capacity to switch between relatively stable and unstable states is key to the reorganization of the microtubule network that occurs between interphase and mitosis, and which enables assembly of the mitotic spindle upon which chromosomes are segregated. Microtubule dynamics are dependent on the intracellular concentration of tubulin, the rate of guanosine triphosphate (GTP) hydrolysis by the tubulin heterodimers, and the activity of numerous microtubule-associated proteins (MAPs) that bind the tips and lateral surface of microtubules (*2-5*).

One family of MAPs that remains relatively poorly characterized is the EMAP-like, or EML, proteins. EMAP (for echinoderm MAP) was first identified in unfertilized sea urchin eggs as the major non-tubulin component of the mitotic spindle (*6, 7*). However, EMLs are highly conserved and have been described in a variety of organisms, including flies, worms and humans (*8-10*). Although their association with microtubules has been shown in different systems, their function in regulating microtubule dynamics remains unclear with studies to date suggesting that different family members might contribute to stabilization and/or destabilization of microtubules (*11-13*). Nevertheless, a delay in mitotic chromosome congression observed upon depletion of EML3 or EML4 in human cells confirms their importance for cell division and supports roles for members of the EML family in spindle organization (*14, 15*).

Six human EMLs have been described (EML1 to EML6), with EML1 to EML4 sharing a similar organization of an N-terminal domain (NTD) of approximately 175-200 residues encompassing a coiled-coil motif and a C-terminal domain of approximately 650 residues consisting of WD (Trp-Asp) repeats (*16*) (Fig. 1A). Crystallographic studies have revealed that the coiled-coil motif forms a homotrimer, referred to as the trimerization domain (TD), while the WD-repeats assemble into two juxtaposed seven-bladed β-propellers, named the TAPE domain for tandem atypical β-propellers in EMLs (*17, 18*). A strongly conserved HELP (hydrophobic EMAP-like protein) motif located towards the start of the TAPE domain provides key residues at the interface between the two β-propellers necessary for proper folding. The TAPE domain in isolation does not localize to microtubules although it does bind tightly to soluble tubulin. Inter-digitation of the two β-propellers generates a curved sheet with a concave and convex surface; the concave surface shares considerable homology between the different EMLs and point mutations in this region disrupt tubulin binding (*17*). Microtubule binding is conferred by the NTD and requires both the TD and a basic region that lies between the TD and start of the TAPE domain. Interestingly, EML5 and EML6 lack the NTD

but have three contiguous copies of the TAPE domain. Hence, whereas EML1 to EML4 can assemble into trimeric complexes that together contain three TAPE domains, EML5 and EML6 contain three copies of the TAPE domain encoded within a single polypeptide. However, because they lack the NTD, it remains unclear whether EML5 and EML6 can bind microtubules.

EML proteins have attracted considerable interest from the cancer community since discovery of translocations involving the genes encoding EML1 and EML4. An EML1-ABL1 fusion protein has been identified in T-cell acute lymphoblastic leukaemia although the frequency appears rare (*19*). In contrast, the EML4-ALK fusion protein is present in a substantial proportion (~5%) of lung adenocarcinoma patients, as well as breast and colorectal tumors (*20-22*). Both ABL1 (Abelson 1) and ALK (anaplastic lymphoma kinase) are tyrosine kinases and fusion of the C-terminal catalytic domain of the kinases to the N-terminal region of the EMLs leads to constitutive kinase activation as a consequence of TD-mediated oligomerization (*23*). Intriguingly, different breakpoints in the EML4 gene lead to distinct EML4-ALK variants that are associated with variable disease progression and therapeutic response in different patients (*24*). EML1 is also implicated in the pathology of an inherited developmental brain disorder where point mutations in the EML1 TAPE domain that potentially destabilize the protein cause neuronal heterotopia in both rodents and humans (*25*).

The microtubule cytoskeleton undergoes dramatic reorganization upon entry into mitosis with a switch from long, relatively stable microtubules to short, unstable microtubules. This switch is largely driven through a change in the complement of MAPs associated with microtubules and significant changes in microtubule nucleation capacity (*26*). Observations that both sea urchin EMAP and human EML4 undergo phosphorylation during mitotic progression suggest that regulation of EML proteins may contribute to these changes in the microtubule network (*27, 28*). EML2, EML3 and EML4 were identified in a large-scale proteomic analysis of human NEK6 binding proteins (*29*). NEK6, and the closely related protein NEK7, are cell cycle-dependent serine/threonine kinases that are activated in mitosis, downstream of another member of this kinase family, NEK9 (*30-33*). NEK9 is a dimeric protein that is phosphorylated in its non-catalytic C-terminal domain by the mitotic kinase, CDK1. This creates a binding site for another mitotic kinase, PLK1, which phosphorylates the catalytic domain of NEK9 activating it in mitosis. Activated NEK9 then undergoes autophosphorylation at a different site in its non-catalytic domain that allows direct binding of NEK6 or NEK7. NEK9 can subsequently activate NEK6 and NEK7 through both direct phosphorylation, and through promoting their dimerization and autophosphorylation. The use of catalytically inactive mutants has shown that activation of NEK6, NEK7 and NEK9 in mitosis is essential for bipolar spindle assembly and efficient chromosome congression (*14, 34-36*).

Here, using antibodies against the endogenous protein, we set out to explore how EML4 might be regulated through the cell cycle. We not only show that the microtubule affinity of EML4 is reduced in mitosis but also that this results from phosphorylation by the NEK6 and NEK7 kinases in the N-terminal microtubule-binding region. We present biochemical and structural data to show that association of EML4 with microtubules occurs through electrostatic interactions between a basic region within EML4 and the acidic tubulin C-terminal tails. Finally, we demonstrate that EML4 is a microtubule stabilizing protein and its displacement from spindle microtubules is essential for chromosome congression in mitosis.

RESULTS

Association of EML4 with microtubules is reduced in mitosis

To examine whether the subcellular localization of EML4 is regulated in a cell cycle-dependent manner two different EML4 antibodies were used. The first detects the N-terminal region between residues 150 and 200, whereas the second detects the C-terminus between residues 951 and 981 (Fig. 1A). Antibody specificity was confirmed by detection of a band at the expected size for EML4 (120 kDa) by Western blot analysis and loss of this band upon depletion of EML4 with two distinct small interfering RNA (siRNA) oligonucleotides (Fig. 1B). Likewise, confocal microscopy with these two antibodies revealed cytoplasmic staining that co-localised with microtubules in human U2OS osteosarcoma cells and that was lost upon depletion of EML4 (Fig. 1C, D). Strikingly, comparison of EML4 localization in interphase and mitotic cells with these antibodies revealed that although the protein was strongly detected on the microtubule network in interphase, it was difficult to detect on spindle microtubules in mitosis (Fig. 1E, F). Quantification revealed an approximate two-fold reduction in co-localization of EML4 with microtubules in metaphase compared to interphase (Fig. 1G, H). A similar loss of association with microtubules was observed for recombinant EML4 upon transition from interphase to mitosis in U2OS cells stably expressing YFP-tagged EML4 (Fig. 1I, J), supporting the hypothesis that affinity of EML4 for microtubules is reduced in mitosis.

The EML4 NTD is phosphorylated in mitosis

To explore how this cell cycle-dependent change in microtubule affinity is regulated, we first examined whether the endogenous EML4 protein was modified upon mitotic entry. Although Western blot analysis revealed no change in abundance of EML4 between extracts prepared from interphase and mitotic HeLa and U2OS cells, there was a distinct reduction in electrophoretic mobility in mitosis compared to interphase in both cell types (Fig. 2A). We then tested which region of the EML4 protein was required for microtubule binding and, as previously shown for EML1 (*18*), confirmed that this property is conferred by the NTD (residues 1-207) and not the TAPE domain (residues 208-878) of EML4 (Fig. 2B, C). Notably,

the isolated EML4 NTD not only co-localised very efficiently with microtubules, but also led to formation of extensive microtubule bundles in the cytoplasm, a phenotype not seen upon expression of the full-length (FL) EML4 protein. As microtubule association is dependent on the EML4 NTD, we asked whether a similar cell cycle-dependent change in gel mobility was detected upon expression of the isolated NTD. Whereas no change in migration was observed for YFP alone, the YFP-tagged EML4-NTD migrated as two distinct bands in lysates prepared from mitotic cells as compared to a single band in interphase cell lysates (Fig. 2D). This suggests that a substantial proportion (~25-30%) of the EML4 NTD is modified upon entry into mitosis. To confirm that this gel-shift was the result of phosphorylation, we treated lysates taken from mitotic cells expressing the YFP-EML4-NTD protein with λ-protein phosphatase and observed a dose-dependent loss of the slower migrating form confirming that this is a phosphorylated version of the EML4-NTD protein (Fig. 2E). The fact that only a fraction of the recombinant protein is phosphorylated is consistent with ectopic expression of the EML4-NTD saturating the cellular kinase(s) responsible for this modification.

Phosphorylation of EML4 by NEK6 and NEK7 regulates its microtubule affinity

To determine which kinase(s) may be responsible for this phosphorylation, we took advantage of the previous observation of an interaction between EML4 and the mitotic NEK6 and NEK7 kinases (*29*). We incubated full-length human EML4 protein purified from insect cells with recombinant NEK6 or NEK7 kinase and ATP. The EML4 proteins were then excised from an SDS-polyacrylamide gel and subjected to mass spectrometry. This revealed four sites that were phosphorylated by NEK6 (Ser^{144}, Thr^{490}, Thr^{609}, Ser^{981}) and four sites phosphorylated by NEK7 (Ser^{134}, Ser^{146}, Thr^{609}, Ser^{981}) (Fig. 3A, and fig. S1). Analysis of published phosphoproteome data on EML4 through PhosphoSitePlus® revealed clustering of phosphorylation within the NTD and at the extreme C-terminus. Of the three sites within the NTD phosphorylated by NEK6 and NEK7, Ser^{134}, Ser^{144} and Ser^{146}, the latter two were by far the most commonly reported serine/threonine phosphorylation sites based on high throughput proteomic discovery mass spectrometry. Moreover, Ser^{144} and Ser^{146}, but not Ser^{134}, are conserved across vertebrate species and, in most cases, have a hydrophobic residue at position -3, typical of NEK6 and NEK7 phosphorylation sites (*37, 38*) (Fig. 3B). We therefore focused on the potential importance of these two sites and generated single S144A and S146A phosphonull mutants, as well as a combined S144/146A double mutant, in constructs expressing YFP-tagged EML4 NTD. Western blot analysis of lysates from transfected U2OS cells revealed no substantial change in migration of the upper band with the single mutants in cells arrested in mitosis. However, the S144/146A double mutant exhibited a much reduced gel-shift confirming that phosphorylation of these two sites is likely to be responsible for the reduced gel mobility in mitotic cells (Fig. 3C). An S144/146A double mutant was therefore also generated in a construct expressing YFP-tagged full-length EML4. Notably, whereas the wild-type EML4 protein did not obviously localise to spindle microtubules, the S144/146A

double mutant very clearly did (Fig. 3D, E). Conversely, a double phosphomimetic EML4-S144/146D mutant associated less well with microtubules than the wild-type protein in interphase cells (fig. S2A, B). Hence, we conclude that phosphorylation at S144 and S146 reduces the affinity of EML4 for microtubules.

To determine if NEK6 and NEK7 can regulate the association of EML4 with microtubules, these kinases were depleted from U2OS cells and the migration of YFP-EML4-NTD analysed in mitotic lysates by Western blot. This revealed that depletion of NEK6, NEK7 or the upstream NEK9 kinase that is responsible for activating NEK6 and NEK7, or chemical inhibition of CDK1 that operates upstream of NEK9, all led to substantial loss of the slower migrating form of the EML4-NTD protein (Fig. 3F, and fig. S2C). Furthermore, analysis of endogenous EML4 by immunofluorescence microscopy revealed that depletion of NEK6, NEK7 or NEK9 led to increased association of EML4 with spindle microtubules (Fig. 3G, H). Depletion of NEK9 led to an increase above that of NEK6 or NEK7 depletion alone. Conversely, expression of constitutively active mutants of NEK6 (Y108A), NEK7 (Y97A) or NEK9 (ΔRCC1) in U2OS cells led to a significant reduction in association of endogenous EML4 with interphase microtubules (fig. S2D, E). However, the reduction of EML4 association with interphase microtubules upon expression of constitutively active NEK9 was unaffected by addition of the CDK1 inhibitor supporting the notion that NEK9 acts downstream of CDK1 (fig. S2F). Together, these data provide persuasive evidence that NEK6 and NEK7, acting downstream of NEK9 and CDK1, regulate microtubule association of EML4 through phosphorylation of residues in its NTD.

The EML NTD binds microtubules through interaction with tubulin C-terminal tails

In EML1, it was shown that the TD and a basic sequence that lies between the TD and TAPE domain confers microtubule binding to EMLs (*18*). The region between the TD and TAPE domain is also highly basic in the EML4 protein (residues 64-207; pI=10.23) and so we hypothesized that association may depend upon electrostatic interaction between this basic region and the acidic surface of the microtubule created by the C-terminal tails of α- and β-tubulin. These C-termini protrude on the exterior surface of the microtubule and are rich in glutamate (E) residues. A number of MAPs associate, at least in part, through interaction of basic domains with these so-called tubulin “E-hooks”, including MAP2 and tau (*39*). To seek evidence that the basic nature of the EML4 NTD mediates microtubule association, the tubulin C-terminal tails of microtubules were removed by limited proteolysis with subtilisin. SDS-PAGE analysis confirmed that tubulin now migrated as a doublet following subtilisin treatment indicative of partial cleavage of the C-terminal tails (Fig. 4A). When incubated with two different concentrations of purified EML4-NTD protein, there was a marked reduction in sedimentation of this protein with the subtilisin-treated microtubules as compared to untreated

microtubules (Fig. 4A-C). We planned to use TIRF microscopy of fluorescently labelled proteins to confirm this dependence on the tubulin C-terminal tails. However, it proved impossible to generate a purified version of fluorescently tagged EML4-NTD protein. We therefore undertook this analysis with a purified YFP-EML1-NTD fragment (residues 1-174). Using a mixed population of untreated microtubules labelled with a 561 nm fluorophore and subtilisin-treated microtubules labelled with a 640 nm fluorophore, we found that the EML1-NTD protein bound strongly to untreated microtubules but not to microtubules treated with subtilisin (Fig. 4D, E). Together, these data are consistent with the basic N-terminal region of EML proteins associating with the acidic tubulin C-terminal tails on the microtubule surface.

Cryo-electron microscopy reveals binding of EML4 to C-terminal tubulin tails

To examine this interaction of the EML4 NTD with microtubules in more detail, we first performed structured illumination microscopy (SIM) of endogenous EML4 in U2OS cells. This revealed small, evenly sized puncta of EML4 distributed along the surface of the cytoplasmic microtubules (Fig. 5A, B). There was no obvious concentration at microtubule ends as has been seen for plus-tip tracking proteins, such as the EBs or ch-TOG proteins (*5*). We then used cryo-electron tomography to directly visualize purified EML4-NTD bound to microtubules in vitro. Low-resolution reconstructions showed density corresponding to EML4-NTD bound along the microtubule outer surface consistent with the SIM analysis of endogenous EML4 in cells (Fig. 5C). It also revealed that while there is occasional evidence of evenly spaced interactions with the microtubules every 4 nm (corresponding to tubulin monomers), binding of EML4-NTD is overall rather disordered. We processed images of EML4-NTD bound to MTs using single particle averaging algorithms, and revealed additional density on both α- and β-tubulin due to bound EML4-NTD (Fig. 5D, E, and fig. S3A-D). Although the resolution of tubulin in our reconstruction is better than 4 Å (Table 1) and shows clear evidence of discrimination between α- and β-tubulin, density corresponding to EML4-NTD is present at substantially lower resolution. This EML4-NTD density lies above the C-terminal helices H11 and H12 of each tubulin monomer, next to where the C-terminal tails of each monomer emerge from the microtubule wall. This confirms the biochemical evidence for involvement of tubulin C-terminal tails in EML4-NTD binding. The low resolution of the EML4-NTD density and the limited extent of density that is visualized is likely due to the flexible nature of its interaction with the tubulin C-terminal tails, which themselves are unstructured and rarely visualised in cryo-EM reconstructions.

Depletion of EML4 reduces stability of interphase microtubules

As microtubules exhibit reduced stability in early mitosis, the loss of EML4 from microtubules at this time could be important for these altered dynamics. This would be consistent with a previous report that overexpression of EML4 stabilises microtubule in Cos7 monkey cells

(*11*). To test whether endogenous EML4 promotes microtubule stability in human cells, we first examined the consequences of depleting EML4 in U2OS cells on the sensitivity of microtubules to the depolymerizing agent, nocodazole. Incubation of mock-depleted cells with 75 nM nocodazole did not affect microtubule organization; however, this dose led to loss of an intact microtubule network in EML4-depleted cells (Fig. 6A). Furthermore, EML4 depletion led to reduced sedimentation of microtubules in the presence of 10 μM taxol, also suggestive of impaired stability (Fig. 6B, C). Stable microtubules are subject to more post-translational modifications, including acetylation and detyrosination. Indeed, depletion of EML4 led to significant reduction of both these markers as measured by Western blot or immunofluorescence microscopy (Fig. 6D-F, and fig. S4). Conversely, time-lapse imaging of live cells incubated with the fluorescent SiR-tubulin probe demonstrated that mitotic spindle microtubules were more resistant to nocodazole-induced depolymerisation upon transient expression of YFP-EML4-S144/146A as compared to wild-type YFP-EML4 protein (Fig 6G, H). Together, these data confirm that binding of EML4 promotes microtubule stabilization and provide a rationale for why it is removed from microtubules upon mitotic entry.

Phosphorylation of the EML4 NTD is required for efficient chromosome congression

To directly test the importance of EML4 displacement from microtubules by phosphorylation in mitosis, we undertook time-lapse confocal imaging of HeLa cells expressing either the wild-type or phosphonull EML4 mutant. These cells also stably express an EGFP-lamin A construct that labels the nuclear envelope and an mCherry-histone H2B construct that labels the chromatin enabling visualization of nuclear envelope breakdown and chromosome dynamics. Whereas in untransfected cells, nuclear envelope breakdown (NEBD) was quickly followed by chromosome congression and anaphase onset (as indicated by sister chromatid separation), these events were delayed in cells expressing the wild-type EML4 protein (Fig. 7A-C). Again this can be explained by overexpression of EML4 saturating the machinery required to regulate its localization. However, expression of the phosphonull S144/146A double mutant protein led to notable failure of both chromosome congression and anaphase onset with less than 30% cells successfully completing cell division after 4 hours in mitosis (Fig. 7A-C). Fixed imaging of U2OS cells arrested in mitosis with MG132 to prevent anaphase onset revealed that 90% of untransfected cells and 75% of cells transfected with wild-type EML4 had condensed chromosomes that were fully aligned on the metaphase plate; in contrast, only 20% of cells transfected with the EML4-S144/146A mutant had fully congressed chromosomes (Fig. 7D, E). Moreover, staining for the microtubule network revealed that the spindle microtubules in these cells were unusually long (Fig. 7D). Finally, we tested whether the mitotic delay in cells expressing the phosphonull EML4 mutant was the result of activation of the spindle assembly checkpoint (SAC). Increased recruitment of the SAC component, BUBR1, to chromatin-associated foci and loss of the mitotic delay upon treatment of cells with an inhibitor of the MPS1 kinase that is essential for SAC activity

confirmed SAC activation in cells expressing the phosphonull EML4 mutant (Fig. 7F-H). Thus, the kinase-dependent displacement of EML4 from microtubules in mitosis is necessary for assembly of a functional mitotic spindle capable of efficient chromosome congression and satisfaction of the SAC.

DISCUSSION

Human EML4 is phosphorylated on serine/threonine residues in mitosis (*27*). Here, we show that EML4 undergoes phosphorylation at Ser^{144} and Ser^{146} in the N-terminal microtubule-binding region in mitosis and that this reduces its affinity for microtubules. This phosphorylation is catalysed by the NEK6 and NEK7 kinases and perturbs electrostatic binding of the EML4 protein with the tubulin C-terminal tails that extend from the surface of the microtubule lattice (Fig. 8A). Confocal and super-resolution microscopy indicate the presence of EML4 foci that are distributed along the length of polymerised microtubules. However, the molecular details of how EML proteins bind microtubules had remained unclear. Our data suggest that this interaction most likely occurs through electrostatic interaction of the basic N-terminal domain of EML4 with the acidic tubulin C-terminal tails (so-called E-hooks) that are exposed on the surface of the microtubule. This conclusion is based not simply on the fact that phosphorylation - the addition of negative charge - weakens the interaction, but on the observation that limited proteolysis of the microtubules with subtilisin that cleaves off these C-terminal tails, abrogated binding. Indeed, cryo-electron microscopy and image reconstruction provided definitive evidence that the EML4 NTD binds at the site on the microtubule where the C-terminal tails emerge on both α- and β-tubulin. Furthermore, spacing of the EML4 NTD foci suggests that the protein can bind to both tubulin monomers within an individual heterodimer. It will be intriguing to further explore the way in which the acidic C-terminal tails from tubulin interact with the trimerised EML4 NTD and how variations in tubulin isoforms and/or post-translational modifications affect this interaction (Fig. 8B). What is also not yet clear is whether the full-length EML4 protein binds in an identical manner and how the TAPE domain, which binds soluble tubulin heterodimers, is oriented with respect to the microtubule.

The mechanism by which EML4 stabilizes microtubules in cells, either directly or indirectly, also remains enigmatic. However, EML4 shares many features with the ch-TOG (XMAP215) family of MAPs in that both proteins have separable domains for binding the microtubule lattice and soluble tubulin. ch-TOG acts as a processive microtubule polymerase by binding to the microtubule with a basic region and then using its multiple TOG domains to add soluble tubulin to the growing microtubule plus-ends (*40, 41*). However, although EML4 has a basic NTD that binds the microtubule polymer and a TAPE domain that binds soluble tubulin, there was no detectable concentration of EML4 at plus ends of microtubules where it could promote

growth through acting as a microtubule polymerase. Interestingly, like tau, EML4 is abundant in the nervous system suggesting that it may have a major function in stabilizing the long microtubules present in neurons (*11*). At the molecular level, proteins of the tau family bind to more than one tubulin dimer, thereby preventing catastrophe, slowing shrinkage and promoting rescue, while also being displaced from the microtubule lattice by phosphorylation (*3, 4*). The fact that EML4 exists as a trimer could allow it to bind to more than one tubulin dimer, thereby increasing its overall avidity for the microtubule surface, and potentially directly stabilising the polymer. However, in contrast to tau (*42*), EML4 does not interact precisely with the microtubule surface but it rather loosely and flexibly associates with the tubulin C-terminal tails. Also in contrast to tau and its relatives, EML2 and the echinoderm EMAP have been reported to destabilise microtubules by increasing the catastrophe rate and decreasing the rescue rate, respectively (*12, 13*). In this regard, it is interesting that the non-neuronal isoform of EML2 used in that study, as well as EMAP, lack the trimerization domain raising the possibility that trimerization is necessary for EMLs to stabilise microtubules. Conversely, a longer isoform of EML2 that does have a trimerization domain is found in the brain and spinal cord (*43*), where it could also stabilize microtubules.

Another key finding of this study is the discovery of a new role for the mitotic NEK6 and NEK7 kinases. Depletion of NEK6 or NEK7, or the upstream kinase NEK9 that activates NEK6 and NEK7 upon mitotic entry, leads to increased association of EML4 with spindle microtubules. This provides compelling evidence that these enzymes play a central role in regulating the microtubule binding affinity of EML4. This hypothesis is supported by the observation that expression of constitutively active mutants of NEK6, NEK7 or NEK9 reduces binding of EML4 to microtubules in interphase. Interestingly, previous depletion and overexpression studies have shown that NEK7 increases the overall dynamicity of interphase microtubules supporting a role for NEK7 in regulating microtubule dynamics in interphase as well as mitosis (*44*). We found that NEK6 and NEK7 were capable of phosphorylating EML4 in vitro, including at Ser^{144} and Ser^{146}, whereas mutation of these two sites or depletion of NEK6, NEK7 or NEK9 led to loss of a gel-mobility shift of the EML4-NTD in mitosis. Together with the fact that EML4 is present in a complex with NEK6 and NEK7 in cells (*29*), this strongly suggests that EML4 is a direct physiological substrate for these kinases. However, we do not exclude the possibility that EML4 may also be subject to additional phospho-dependent regulation by other mitotic, as well as non-mitotic, kinases. Indeed, the sea-urchin EMAP protein was found to be efficiently phosphorylated by CDK1 (*28*). We also observed loss of the gel-mobility shift of the EML4-NTD in mitosis upon addition of a CDK1 inhibitor, but this result can be explained by CDK1 acting upstream of NEK9. Indeed, the CDK1 inhibitor did not prevent activated NEK9 displacing EML4 from interphase microtubules adding weight to the conclusion that EML4 can be regulated in human cells by the NEK9-NEK6-NEK7 module. Interestingly, analysis of the PhosphoSitePlus® database suggests that while Ser^{144} and Ser^{146} are the two most commonly detected serines or threonines phosphorylated in EML4,

there is even more frequent detection of phosphorylation at Tyr^{226}. This residue sits at the junction of the NTD and TAPE domain and it will be interesting in the future to test the role of this phosphorylation on EML4 function.

Depletion of NEK6 or NEK7 disrupts spindle formation in mitosis and both the kinesin Eg5 and the chaperone HSP72 have been reported as mitotic substrates of NEK6 (*35, 45*). Our work here indicates that EML4 should be added to that growing list of substrates for these kinases and that, like CDK1, PLK1 and Aurora-A, the mitotic NEKs phosphorylate multiple substrates to drive robust spindle assembly. Removal of EML4 from microtubules appears to be crucial for the decrease in stability that accompanies assembly of a highly dynamic mitotic spindle. Live cell imaging demonstrated not only that microtubules were more stable but also that the ability of condensed chromosomes to congress to the metaphase plate was severely hampered in cells expressing a phosphonull EML4 mutant. This was accompanied by a delay in anaphase onset that was mediated by persistent activity of the SAC as evidenced by kinetochore recruitment of the SAC component, BUBR1, and loss of this delay upon addition of an MPS1 inhibitor, which abrogates the SAC. Interestingly, EML4 is nevertheless required for mitotic progression arguing that, despite the reduced microtubule binding affinity, it still plays an important role at this stage of the cell cycle. EML4 was found to bind the nuclear distribution C (NUDC) protein via its TAPE domain and target NUDC to the spindle promoting kinetochore capture by microtubules (*15*). Whether this requires the microtubule binding activity of EML4 is not known. Of course, while microtubule stability initially drops upon mitotic entry during the process of search-and-capture, specific populations of microtubules, notably K-fibres, become highly stabilised upon bi-orientation of chromosomes (*46*). Indeed, residual staining of spindle microtubules was detected and it is plausible that EML4 could yet contribute to K-fibre stability if a localized fraction of EML4 was dephosphorylated.

Many proteins specifically interact with microtubules during mitosis. These fulfil a variety of important functions that include the regulation of microtubule stability, the trafficking of checkpoint complexes, and the motility of the condensed chromosomes (*47*). Collectively, these proteins enable the assembly of a dynamic and finely tuned mitotic spindle. In contrast, EML4 preferentially interacts with microtubules during interphase, and the regulated disruption of this interaction through phosphorylation is what is necessary for proper mitotic spindle assembly and function. This raises the question of how many other proteins might dissociate from microtubules during mitosis. Indeed, it seems likely that the electrostatic interactions that other microtubule-associated proteins depend on might also be disrupted through phosphorylation, as protein phosphorylation peaks during this phase of the cell cycle. This mode of regulation could therefore be relevant to other proteins, including potentially other members of the EML family, that interact with the negatively charged tubulin C-terminal tails.

MATERIALS AND METHODS

Plasmid construction, mutagenesis and recombinant protein expression

Generation of YFP-EML4-FL and YFP-EML1-NTD constructs was previously described (*18*), while YFP-EML4-NTD and YFP-EML4-TAPE were generated by PCR-based amplification of the NTD and TAPE domain fragments from the YFP-EML4-FL plasmid and subcloning into pLEICS-12 (PROTEX, University of Leicester). Generation of Flag-NEK6-Y108A, Flag-NEK7-Y97A, and Flag-NEK9-ΔRCC1 constructs were as described (*31, 32, 34*). Mutations were introduced into the YFP-EML4-FL and NTD constructs using the GeneTailor Site-Directed Mutagenesis Kit (Invitrogen), and all constructs confirmed by Sanger sequencing at the University of Leicester. The YFP-EML1-NTD and YFP-EML4-NTD proteins were expressed and purified as described (*18*), while Flag-Strep-EML4-FL protein used for phosphomapping was expressed in insect cells and purified as described(*17*).

Cell culture, transfection and drug treatment

U2OS, HeLa and HEK 293 cells were grown in Dulbecco's modified Eagle's medium (DMEM, Invitrogen) supplemented with 10% heat-inactivated foetal bovine serum (FBS), 100 IU/ml penicillin and 100 µg/ml streptomycin at 37^0C in a 5% CO_2 atmosphere. HeLa Kyoto H2B-mCherry/EGFP-Lamin A cells were maintained in DMEM containing 10% FBS, 100 IU/ml penicillin, 100 µg/ml streptomycin, 500 µg/ml G418 and 0.5 µg/ml puromycin. Transient transfections were performed with Lipofectamine 2000 (Invitrogen) according to manufacturer's instructions. Cells were synchronized in M-phase either by incubation for 16 hours with 500 ng/ml nocodazole, or by incubation with 10 µM RO-3306 (Enzo Life Science) for 16 hours followed by transfer into fresh media with 20 µM MG132 (EMD Millipore) for 2 hours. M-phase arrested cells were collected by mitotic shake-off after 16 hours treatment. SAC inactivation was achieved through incubation with the MPS1 inhibitor, AZ3146 (Sigma), for 4 hours.

Western blotting

Cells were lysed in ice-cold RIPA or NEB lysis buffer (50 mM Tris-HCl pH 8, 150 mM NaCl, 1% v/v Nonidet P-40, 0.1% w/v SDS, 0.5% w/v sodium deoxycholate, 5 mM NaF, 5 mM β-glycerophosphate, 30 µg/ml RNase, 30 µg/ml DNase I, 1x Protease Inhibitor Cocktail, 1 mM PMSF) and subjected to SDS-PAGE and analysis by Western blotting. Primary antibodies were rabbit NEK6 (1 µg/ml; (32), goat NEK7 (1:250; Aviva Systems), rabbit NEK9 (0.4 µg/ml; Atlas Antibodies), mouse α-tubulin (0.3 µg/ml; Sigma), mouse acetylated tubulin (1:2000; Sigma), rabbit GAPDH (1:500; Cell Signaling), rabbit EML4 (N-term, A301-908A; C-term, A301-909A; both 1:500, Bethyl Laboratories), rabbit green fluorescent protein (GFP; 0.5

µg/ml; Abcam), mouse pHistone H3 (1:1000, Abcam) and mouse cyclin B1 (0.5 µg/ml; Santa Cruz). Secondary antibodies were horseradish peroxidase (HRP)-labelled secondary antibodies (1:1000; Amersham).

RNAi

Cells at 30–40% confluency were cultured in Opti-MEM Reduced Serum Medium with 10% heat-inactivated foetal bovine serum (FBS), and transfected with 50 nM ON-TARGETplus siRNA duplexes using Oligofectamine (Invitrogen) according to manufacturer's instructions. siRNA duplexes were as previously described for NEK6 and NEK7 (*34*), NEK9 (AM51334-1113, Ambion) and EML4 (HSS120688 and HSS178451, Dharmacon). Cells were fixed or lysed for analysis after 72 hours transfection.

In vitro kinase assay and mass spectrometry

Kinase assays were carried out using 0.1 µg purified NEK6 or NEK7 kinase (Millipore). Proteins were incubated with 5 µg substrate and 1 µCi of [γ-32P]-ATP in 40 µl kinase buffer (50 mM Hepes.KOH pH 7.4, 5 mM $MnCl_2$, 5 mM β-glycerophosphate, 5 mM NaF, 4 µM ATP, 1 mM DTT) at 30^0C for 30 mins. Reactions were stopped with 50 µl of protein sample buffer and analysed by SDS-PAGE and autoradiography. Phosphomapping was performed using an LTQ-Orbitrap-Velos-ETD (ThermoFisher Scientific) as previously described (*35*).

Fluorescence microscopy

For immunofluorescence microscopy, cells were grown on acid-etched glass coverslips, fixed with ice-cold methanol or methanol: acetone (1:1) and processed as previously described (*34*). In brief, media were aspirated and cells fixed with ice-cold methanol at -20^0C for 30 mins. Cells were blocked in 1x PBS supplemented with 3% BSA and 0.2% Triton X-100 before incubation with antibodies in 1x PBS supplemented with 3% BSA. Primary antibodies used were mouse α-tubulin (0.3 µg/ml; Sigma-Aldrich), rabbit Flag (1:1000; Sigma-Aldrich), rabbit green fluorescent protein (GFP) (1 µg/ml; Abcam), rabbit EML4 (N-term, A301-908A; C-term, A301-909A; both 1:500, Bethyl Laboratories), mouse acetylated tubulin (1:2000; sigma), goat Flag (1:1000; Abcam), and rat α-tubulin conjugated 647 (1:200; Abcam). Secondary antibodies used were Alexa Fluor 488, 594 and 647 donkey anti-rabbit, donkey anti-mouse and donkey anti-goat IgGs (1 µg/ml; Invitrogen). DNA was stained with 0.8 µg/ml Hoechst 33258. Fixed and time-lapse imaging were performed on a Leica TCS SP5 confocal laser scanning microscope fitted on a Leica DMI 6000B inverted microscope using a hcx plan apo 63x oil objective (numerical aperture, 1.4). For fixed images, Z stacks comprising 30–50 0.3 µm sections were acquired using LAS-AF software (Leica), and deconvolution of 3D image stacks performed using Huygens Essential software (Scientific Volume Imaging). For

time-lapse fluorescence imaging, cells were cultured in glass-bottomed culture dishes (MatTek Corporation) and maintained on the stage at 37°C in an atmosphere supplemented with 5% CO_2 using an environmental chamber (Life Imaging Services). Z-stacks comprising of 0.5 µm sections were acquired every 10 min for a minimum of 16 h. Stacks were processed into maximum intensity projections using LAS-AF software (Leica) and movies prepared using ImageJ. To quantify colocalization, ImageJ software was used to draw five lines across the cytoplasmic regions of a cell on a single z-section of an image. A total of 10 cells from three independent experiments were used to calculate the mean Pearson's correlation coefficient (R-value).

For structured illumination microscopy (SIM), cells were grown on acid-etched high performance coverslips, fixed in ice-cold methanol and stained for immunofluorescence microscopy with EML4 and α-tubulin antibodies as described above. However, following incubation with the secondary antibody, cells were subjected to a second, post-fixation step in which cells were incubated with 4% paraformaldehyde for 10 mins, prior to coverslips being mounted onto microscope slides with Citifluor mounting medium (Electron Microscopy Sciences). Imaging was performed using a Zeiss PS1 super resolution microscope and images processed using Zen software (Zeiss).

For TIRF imaging, microtubules were prepared from a mixture of 2 µM biotin-labelled, 2 µM Hilyte647-labelled and 20 µM unlabelled tubulin, 1 mM GMP-CPP in MRB80 (80 mM K-PIPES, 4 mM $MgCl_2$, 1 mM EGTA, pH 6.9). Microtubules were then treated with subtilisin (25 µg/ml) or left untreated and incubated for 20 mins at 37°C. To terminate digestion 2 mM PMSF was added and the reaction mix centrifuged for 5 mins at 150,000 xg. The supernatant was removed and microtubules re-suspended in MRB80 buffer. Microtubules were attached to the surface of a flow cell using PLL-PEG-biotin and streptavidin, and binding of 100 nM recombinant EML1 (1-174) was assessed using TIRF microscopy as described (*18*).

In vitro microtubule binding and sedimentation assays

Microtubules were assembled from 40 µM tubulin in the presence of 5 mM GTP in MRB80 for 1 h at 37ºC, diluted 1:3 in MRB80 + 2 µM Taxol. 3/5 of the sample was treated with 25 µg/ml subtilisin (Sigma P5380) and the remainder left untreated and incubated at 37ºC for 10 min. To terminate digestion 5 mM PMSF and complete protease inhibitors (Roche) were added and the reaction mix loaded onto a 30% sucrose cushion and centrifuged in a TLA55 rotor at 100,000 xg for 45 mins at 30ºC. The microtubule pellets were re-suspended in BRB25 (25 mM PIPES pH 6.8, 1 mM $MgCl_2$, 1 mM EGTA, 2 mM DTT) supplemented with complete protease inhibitors and 2 µM Taxol and incubated with EML4(1-207)-Avi on ice for 15 mins before pelleting through a 30% Sucrose cushion in a TLA55 rotor at 100,000 xg for 45 mins at

4ºC. The pellet was taken up in equal volume to supernatant and samples analysed on 12% SDS-PAGE gels, stained with Instant Blue (Expedion), imaged on a G-Box (Syngene) and quantified using ImageJ.

For microtubule sedimentation assays, cells were lysed at room temperature in RIPA lysis buffer, including 5 mM NaF, 5 mM β-glycerophosphate. Samples were loaded on the top layer of 30% sucrose in tubulin stabilization buffer (TSB; 1 mM EGTA, 5 mM $MgCl_2$, 80 mM PIPES at pH 7.0) before centrifugation at 100,000 g for 40 mins at 21^{o}C. Supernatants were collected and pellets washed with TSB for 10 mins at 21^{o}C. Pellets were diluted into a volume equal to that of the supernatants. Samples were subjected to SDS-PAGE and analysis by Western blot.

Live-cell microtubule stability assays

For measurement of microtubule stability in live cells, U2OS cells were transfected with YFP-EML4-WT or S144/146A for 24 hours prior to being grown in µ-well 8 well chamber slides (Ibidi). Cells were incubated with 25 nM SiR-Tubulin (Cytoskeleton Inc) for 4 hours and MG132 was added to the media 30 min prior to imaging. Fields of view containing transfected cells with bipolar mitotic spindles were selected and media supplemented with 200 µg/ml nocodazole along with MG132 and SiR tubulin, and image capture immediately commenced. Z stacks comprising 29x 0.5 µm sections were captured every 60 s for 15 minutes using a VisiTech infinity 3 confocal microscope fitted with a Hamamatsu C11449-22CU Flash 4.0 V2 sCMOS camera and Nikon Plan Apo 100x objective (NA 1.47). Images were cropped to single cells and deconvolved prior to analysis for Si-R tubulin intensity in Matlab.

Sample preparation for cryo-electron microscopy

Lyophilized tubulin purified from HeLa cells was purchased from Cytoskeleton Inc. (Denver, CO, USA) and reconstituted to 2.5 mg/ml in BRB80 (80 mM PIPES, 1.5 mM $MgCl_2$, 1 mM EGTA, 1 mM DTT) containing 1 mM GMPCPP at 4°C. After 10 mins incubation at 4°C the tubulin was transferred to a water bath and polymerised at 37°C for 45 mins. In order to increase GMPCPP occupancy, microtubules were double-cycled by pelleting at 13,000 rpm on a desktop centrifuge at room temperature, removing the supernatant and re-suspending the microtubule pellet to ~2.5 mg/ml at 4°C in BRB80 + 1 mM GMPCPP. Microtubules were then repolymerised by incubation at 37°C for 45 mins. Stabilised microtubules were left at room temperature for 3 hours then diluted in room temperature BRB25 + 1 mM GMPCPP to 0.5 mg/ml before use (25 mM PIPES, 1.5 mM $MgCl_2$, 1 mM EGTA, 1 mM DTT). 4 µl of microtubules were pre-incubated on glow-discharged holey C-flat^{TM} carbon EM grids (Protochips, Morrisville, NC) at room temperature for 1 min, excess buffer manually blotted away, then 4 µl of 2.2 mg/ml EML4-NTD in BRB25 + 30 mM NaCl and 1 mM GMPCPP added

for 45 sec. Excess buffer was again manually blotted away, followed by another 4 µl application of EML4-NTD. In an additional step for cryo-electron tomography only, excess buffer was again blotted away after 45 sec incubation and 4 µl of 10 nm nanogold fiducial–BSA solution (Sigma), concentrated 2-fold in BRB25 + 30 mM NaCl and 1 mM GMPCPP, added to the grid. Grids were then placed in a Vitrobot Mark IV (FEI Co., Hillsboro, OR) at room temperature and 80% humidity, incubated for a further 45 sec, then blotted and vitrified in liquid ethane.

Single-particle cryo-electron microscopy data collection and processing

Low dose movies were collected automatically using EPU software on a K2 summit direct electron detector (Gatan) installed on a FEI Titan Krios (Astbury Biostructure Laboratory, University of Leeds) operating at 300kV with a quantum post-column energy-filter (Gatan), operated in zero-loss imaging mode with a 20-eV energy-selecting slit. A defocus range of 0.5-2.5µm and a calibrated final sampling of 1.37Å/pixel was used with the K2 operating in counting mode at 6e-/pixel/second. The total exposure was 48e-/Å^2 over 30 frames (1.6e-/Å^2/frame). Movie frames were aligned using MotionCor2 (*48*) with a patch size of 5 to generate full dose and dose-weighted sums. Full dose sums were used for CTF determination in gCTF (*49*), then dose-weighted sums used in particle picking, processing and generation of the final reconstructions. Particle processing was performed with helical methods in RELION v2.1.0 (*50*), using a custom pipeline and scripts to account for microtubule pseudo-helical symmetry. Briefly, microtubules were boxed manually in RELION with a box separation distance of 82Å (roughly the microtubule dimer repeat distance). The protofilament number of all segments within each microtubule was assigned according to the modal class of those segments after one iteration of 3D classification to 12 Å low-pass filtered references of undecorated 11-16-protofilament microtubules built from multiple asymmetric units of the GMPCPP microtubule atomic model (PDB: 6DPU (*51*)). Once the protofilament number of each microtubule had been established, the main 13-protofilament microtubule class was selected for further processing. Rough alignment parameters of each microtubule to its corresponding 7 Å low-pass filtered 13-protofilament reference were assigned. On the basis of φ angles determined for each segment, median φ angles were assigned to all segments in a given microtubule. Assigned φ angles for each microtubule were checked by 3D classification against 7 Å low-pass filtered undecorated 13-protofilament microtubule references rotated and translated to represent all possible seam positions and αβ-tubulin registers. For all references used in this step, pixel values were doubled for atoms within the S9-S10 and H1-S2 loops, being the main distinctive features between α- and β-tubulin. Rough final φ angles were assigned according to the modal 3D class of all segments within each microtubule. Finer local refinement was then performed, with or without applied helical symmetry. Final displayed reconstructions were sharpened to local resolutions as determined in Relion, unless stated. 4 x binned data were used for the protofilament number assignment

3D classification, unbinned data for the final local refinements and 2x binned data for all other steps. The atomic models of 6 dimers of undecorated GMPCPP MTs (PDB: 6DPU) with incorporated taxol (taken from PDB: 5SYF (*52*)) were fitted into symmetrized density and used as starting models for iterative rounds of model building in Coot (*53*) and Phenix (*54*). Extra density contributed by EML4-NTD had low resolution, presumably due to the flexible nature of the MT-EML4-NTD interaction; therefore EML4-NTD was not modelled into density.

Cryo-electron tomography data collection and processing

Single-axis cryo-electron tomography of EML4-NTD decorated microtubules was performed using a Tecnai G2 Polara at 300 kV with a Quantum post-column energy filter (Gatan) operated in zero-loss imaging mode with a 20-eV energy-selecting slit. Data at 5–6 µm defocus were collected on a K2 Summit direct electron detector operating in counting mode at 9e-/pixel/second (measured without sample obstructing the beam) with a final sampling of 5.39Å per pixel. Tilt series of total dose 114e-/Å^2 from -60 to +60˚ tilt were collected in 3˚ increments using the Hagen dose-symmetric tilt scheme (*55*). For each tilt, movies of 9 seconds exposure at four subframes per sec were aligned using MotionCor2 (*48*). Dose weighting of tilt series was performed using custom scripts calling functions in SumMovie (*56*). Fiducial-based alignment of tilt series was performed in the Etomo graphical user interface to IMOD (v.4.9.0). CTF determination on each aligned tilt series without dose-weighting was performed with CTFFIND4 (*57*) and three-dimensional CTF correction and tomogram reconstruction was performed by weighted back-projection of dose-compensated and aligned tilt series with novaCTF (*58*). Final tomograms displayed were 4xbinned using IMOD and a B-factor of 35000 applied to amplify low-frequency information.

Statistical analysis

All quantitative data represent means and standard deviation of at least three independent experiments. Statistical analyses were performed using a one-tailed unpaired Student's t test assuming unequal variance; *, $p<0.05$; **, $p<0.01$; ***, $p<0.001$. n.s., non-significant. For live-cell microtubule stability assays the area under the curve for each data set was calculated and statistical analysis on these values was performed using a one-tailed unpaired Student's t-test assuming unequal variance.

SUPPLEMENTARY MATERIALS

See Supplementary Materials for Supplementary Figures.

REFERENCES AND NOTES

1. A. Desai, T. J. Mitchison, Microtubule polymerization dynamics. *Annu Rev Cell Dev Biol* **13**, 83-117 (1997).
2. J. L. Lawson, R. E. Carazo Salas, Microtubules: greater than the sum of the parts. *Biochem Soc Trans* **41**, 1736-1744 (2013).
3. H. Bowne-Anderson, A. Hibbel, J. Howard, Regulation of Microtubule Growth and Catastrophe: Unifying Theory and Experiment. *Trends Cell Biol* **25**, 769-779 (2015).
4. B. van der Vaart, A. Akhmanova, A. Straube, Regulation of microtubule dynamic instability. *Biochem Soc Trans* **37**, 1007-1013 (2009).
5. A. Akhmanova, M. O. Steinmetz, Control of microtubule organization and dynamics: two ends in the limelight. *Nat Rev Mol Cell Biol* **16**, 711-726 (2015).
6. K. A. Suprenant, K. Dean, J. McKee, S. Hake, EMAP, an echinoderm microtubule-associated protein found in microtubule-ribosome complexes. *Journal of cell science* **104**, 445-450 (1993).
7. K. A. Suprenant, J. C. Marsh, Temperature and pH govern the self-assembly of microtubules from unfertilized sea-urchin egg extracts. *Journal of cell science* **87 (Pt 1)**, 71-84 (1987).
8. K. A. Suprenant, J. A. Tuxhorn, M. A. Daggett, D. P. Ahrens, A. Hostetler, J. M. Palange, C. E. VanWinkle, B. T. Livingston, Conservation of the WD-repeat, microtubule-binding protein, EMAP, in sea urchins, humans, and the nematode C. elegans. *Dev Genes Evol* **210**, 2-10 (2000).
9. S. Bechstedt, J. T. Albert, D. P. Kreil, T. Muller-Reichert, M. C. Gopfert, J. Howard, A doublecortin containing microtubule-associated protein is implicated in mechanotransduction in Drosophila sensory cilia. *Nat Commun* **1**, 11 (2010).
10. J. L. Hueston, G. P. Herren, J. G. Cueva, M. Buechner, E. A. Lundquist, M. B. Goodman, K. A. Suprenant, The C. elegans EMAP-like protein, ELP-1 is required for touch sensation and associates with microtubules and adhesion complexes. *BMC Dev Biol* **8**, 110 (2008).
11. S. H. Houtman, M. Rutteman, C. I. De Zeeuw, P. J. French, Echinoderm microtubule-associated protein like protein 4, a member of the echinoderm microtubule-associated protein family, stabilizes microtubules. *Neuroscience* **144**, 1373-1382 (2007).
12. D. R. Hamill, B. Howell, L. Cassimeris, K. A. Suprenant, Purification of a WD repeat protein, EMAP, that promotes microtubule dynamics through an inhibition of rescue. *J Biol Chem* **273**, 9285-9291 (1998).
13. B. Eichenmuller, P. Everley, J. Palange, D. Lepley, K. A. Suprenant, The human EMAP-like protein-70 (ELP70) is a microtubule destabilizer that localizes to the mitotic apparatus. *J Biol Chem* **277**, 1301-1309 (2002).
14. J. Tegha-Dunghu, B. Neumann, S. Reber, R. Krause, H. Erfle, T. Walter, M. Held, P. Rogers, K. Hupfeld, T. Ruppert, J. Ellenberg, O. J. Gruss, EML3 is a nuclear microtubule-binding protein required for the correct alignment of chromosomes in metaphase. *Journal of cell science* **121**, 1718-1726 (2008).
15. D. Chen, S. Ito, H. Yuan, T. Hyodo, K. Kadomatsu, M. Hamaguchi, T. Senga, EML4 promotes the loading of NUDC to the spindle for mitotic progression. *Cell Cycle* **14**, 1529-1539 (2015).
16. A. M. Fry, L. O'Regan, J. M. Montgomery, R. Adib, R. Bayliss, EML proteins in microtubule regulation and human disease. *Biochem Soc Trans* **44**, 1281-1288 (2016).
17. M. W. Richards, E. W. Law, L. P. Rennalls, S. Busacca, L. O'Regan, A. M. Fry, D. A. Fennell, R. Bayliss, Crystal structure of EML1 reveals the basis for Hsp90 dependence of oncogenic EML4-ALK by disruption of an atypical beta-propeller domain. *Proc Natl Acad Sci U S A* **111**, 5195-5200 (2014).
18. M. W. Richards, L. O'Regan, D. Roth, J. M. Montgomery, A. Straube, A. M. Fry, R. Bayliss, Microtubule association of EML proteins and the EML4-ALK variant 3 oncoprotein require an N-terminal trimerization domain. *Biochem J* **467**, 529-536 (2015).
19. K. De Keersmaecker, C. Graux, M. D. Odero, N. Mentens, R. Somers, J. Maertens, I. Wlodarska, P. Vandenberghe, A. Hagemeijer, P. Marynen, J. Cools, Fusion of EML1

to ABL1 in T-cell acute lymphoblastic leukemia with cryptic t(9;14)(q34;q32). *Blood* **105**, 4849-4852 (2005).
20. M. Soda, Y. L. Choi, M. Enomoto, S. Takada, Y. Yamashita, S. Ishikawa, S. Fujiwara, H. Watanabe, K. Kurashina, H. Hatanaka, M. Bando, S. Ohno, Y. Ishikawa, H. Aburatani, T. Niki, Y. Sohara, Y. Sugiyama, H. Mano, Identification of the transforming EML4-ALK fusion gene in non-small-cell lung cancer. *Nature* **448**, 561-566 (2007).
21. E. Lin, L. Li, Y. Guan, R. Soriano, C. S. Rivers, S. Mohan, A. Pandita, J. Tang, Z. Modrusan, Exon array profiling detects EML4-ALK fusion in breast, colorectal, and non-small cell lung cancers. *Mol Cancer Res* **7**, 1466-1476 (2009).
22. K. Rikova, A. Guo, Q. Zeng, A. Possemato, J. Yu, H. Haack, J. Nardone, K. Lee, C. Reeves, Y. Li, Y. Hu, Z. Tan, M. Stokes, L. Sullivan, J. Mitchell, R. Wetzel, J. Macneill, J. M. Ren, J. Yuan, C. E. Bakalarski, J. Villen, J. M. Kornhauser, B. Smith, D. Li, X. Zhou, S. P. Gygi, T. L. Gu, R. D. Polakiewicz, J. Rush, M. J. Comb, Global survey of phosphotyrosine signaling identifies oncogenic kinases in lung cancer. *Cell* **131**, 1190-1203 (2007).
23. S. R. Sabir, S. Yeoh, G. Jackson, R. Bayliss, EML4-ALK Variants: Biological and Molecular Properties, and the Implications for Patients. *Cancers (Basel)* **9**, E118 (2017).
24. R. Bayliss, J. Choi, D. A. Fennell, A. M. Fry, M. W. Richards, Molecular mechanisms that underpin EML4-ALK driven cancers and their response to targeted drugs. *Cell Mol Life Sci* **73**, 1209-1224 (2016).
25. M. Kielar, F. P. Tuy, S. Bizzotto, C. Lebrand, C. de Juan Romero, K. Poirier, R. Oegema, G. M. Mancini, N. Bahi-Buisson, R. Olaso, A. G. Le Moing, K. Boutourlinsky, D. Boucher, W. Carpentier, P. Berquin, J. F. Deleuze, R. Belvindrah, V. Borrell, E. Welker, J. Chelly, A. Croquelois, F. Francis, Mutations in Eml1 lead to ectopic progenitors and neuronal heterotopia in mouse and human. *Nat Neurosci* **17**, 923-933 (2014).
26. R. Heald, A. Khodjakov, Thirty years of search and capture: The complex simplicity of mitotic spindle assembly. *J Cell Biol* **211**, 1103-1111 (2015).
27. M. Pollmann, R. Parwaresch, S. Adam-Klages, M. L. Kruse, F. Buck, H. J. Heidebrecht, Human EML4, a novel member of the EMAP family, is essential for microtubule formation. *Exp Cell Res* **312**, 3241-3251 (2006).
28. E. Brisch, M. A. Daggett, K. A. Suprenant, Cell cycle-dependent phosphorylation of the 77 kDa echinoderm microtubule-associated protein (EMAP) in vivo and association with the p34cdc2 kinase. *Journal of cell science* **109 (Pt 12)**, 2885-2893 (1996).
29. R. M. Ewing, P. Chu, F. Elisma, H. Li, P. Taylor, S. Climie, L. McBroom-Cerajewski, M. D. Robinson, L. O'Connor, M. Li, R. Taylor, M. Dharsee, Y. Ho, A. Heilbut, L. Moore, S. Zhang, O. Ornatsky, Y. V. Bukhman, M. Ethier, Y. Sheng, J. Vasilescu, M. Abu-Farha, J. P. Lambert, H. S. Duewel, Stewart, II, B. Kuehl, K. Hogue, K. Colwill, K. Gladwish, B. Muskat, R. Kinach, S. L. Adams, M. F. Moran, G. B. Morin, T. Topaloglou, D. Figeys, Large-scale mapping of human protein-protein interactions by mass spectrometry. *Mol Syst Biol* **3**, 89 (2007).
30. C. Belham, J. Roig, J. A. Caldwell, Y. Aoyama, B. E. Kemp, M. Comb, J. Avruch, A mitotic cascade of NIMA family kinases. Nercc1/Nek9 activates the Nek6 and Nek7 kinases. *J Biol Chem* **278**, 34897-34909 (2003).
31. J. Roig, A. Mikhailov, C. Belham, J. Avruch, Nercc1, a mammalian NIMA-family kinase, binds the Ran GTPase and regulates mitotic progression. *Genes Dev.* **16**, 1640-1658 (2002).
32. M. W. Richards, L. O'Regan, C. Mas-Droux, J. M. Blot, J. Cheung, S. Hoelder, A. M. Fry, R. Bayliss, An autoinhibitory tyrosine motif in the cell-cycle-regulated Nek7 kinase is released through binding of Nek9. *Mol Cell* **36**, 560-570 (2009).
33. A. M. Fry, R. Bayliss, J. Roig, Mitotic Regulation by NEK Kinase Networks. *Front Cell Dev Biol* **5**, 102 (2017).
34. L. O'Regan, A. M. Fry, The Nek6 and Nek7 protein kinases are required for robust mitotic spindle formation and cytokinesis. *Mol Cell Biol* **29**, 3975-3990 (2009).
35. L. O'Regan, J. Sampson, M. W. Richards, A. Knebel, D. Roth, F. E. Hood, A. Straube, S. J. Royle, R. Bayliss, A. M. Fry, Hsp72 is targeted to the mitotic spindle by

Nek6 to promote K-fiber assembly and mitotic progression. *J Cell Biol* **209**, 349-358 (2015).
36. M.-J. Yin, L. Shao, D. Voehringer, T. Smeal, B. Jallal, The serine/threonine kinase Nek6 is required for cell cycle progression through mitosis. *J. Biol. Chem.* **278**, 52454-52460 (2003).
37. J. M. Lizcano, M. Deak, N. Morrice, A. Kieloch, C. J. Hastie, L. Dong, M. Schutkowski, U. Reimer, D. R. Alessi, Molecular basis for the substrate specificity of NIMA-related kinase-6 (NEK6). Evidence that NEK6 does not phosphorylate the hydrophobic motif of ribosomal S6 protein kinase and serum- and glucocorticoid-induced protein kinase in vivo. *J Biol Chem* **277**, 27839-27849 (2002).
38. B. van de Kooij, P. Creixell, A. van Vlimmeren, B. Joughin, C. J. Miller, N. Haider, C. D. Simpson, R. Linding, V. Stambolic, B. E. Turk, M. B. Yaffe, Comprehensive substrate specificity profiling of the human Nek kinome reveals unexpected signaling outputs. *Elife* **8**, (2019).
39. S. W. Manka, C. A. Moores, Microtubule structure by cryo-EM: snapshots of dynamic instability. *Essays Biochem* **62**, 737-751 (2018).
40. J. Al-Bassam, F. Chang, Regulation of microtubule dynamics by TOG-domain proteins XMAP215/Dis1 and CLASP. *Trends Cell Biol* **21**, 604-614 (2011).
41. G. J. Brouhard, J. H. Stear, T. L. Noetzel, J. Al-Bassam, K. Kinoshita, S. C. Harrison, J. Howard, A. A. Hyman, XMAP215 is a processive microtubule polymerase. *Cell* **132**, 79-88 (2008).
42. E. H. Kellogg, N. M. A. Hejab, S. Poepsel, K. H. Downing, F. DiMaio, E. Nogales, Near-atomic model of microtubule-tau interactions. *Science* **360**, 1242-1246 (2018).
43. D. M. Lepley, J. M. Palange, K. A. Suprenant, Sequence and expression patterns of a human EMAP-related protein-2 (HuEMAP-2). *Gene* **237**, 343-349 (1999).
44. S. Cohen, A. Aizer, Y. Shav-Tal, A. Yanai, B. Motro, Nek7 kinase accelerates microtubule dynamic instability. *Biochim Biophys Acta* **1833**, 1104-1113 (2013).
45. J. Rapley, M. Nicolas, A. Groen, L. Regue, M. T. Bertran, C. Caelles, J. Avruch, J. Roig, The NIMA-family kinase Nek6 phosphorylates the kinesin Eg5 at a novel site necessary for mitotic spindle formation. *Journal of cell science* **121**, 3912-3921 (2008).
46. A. L. Manning, S. F. Bakhoum, S. Maffini, C. Correia-Melo, H. Maiato, D. A. Compton, CLASP1, astrin and Kif2b form a molecular switch that regulates kinetochore-microtubule dynamics to promote mitotic progression and fidelity. *The EMBO journal* **29**, 3531-3543 (2010).
47. J. G. Ferreira, A. L. Pereira, H. Maiato, Microtubule plus-end tracking proteins and their roles in cell division. *Int Rev Cell Mol Biol* **309**, 59-140 (2014)
48. S. Q. Zheng, E. Palovcak, J. P. Armache, K. A. Verba, Y. Cheng, D. A. Agard, MotionCor2: anisotropic correction of beam-induced motion for improved cryo-electron microscopy. *Nat Methods* **14**, 331-332 (2017).
49. K. Zhang, Gctf: Real-time CTF determination and correction. *J Struct Biol* **193**, 1-12 (2016).
50. S. He, S. H. W. Scheres, Helical reconstruction in RELION. *J Struct Biol* **198**, 163-176 (2017).
51. R. Zhang, B. LaFrance, E. Nogales, Separating the effects of nucleotide and EB binding on microtubule structure. *Proc Natl Acad Sci U S A* **115**, E6191-E6200 (2018)
52. E. H. Kellogg, N. M. A. Hejab, S. Howes, P. Northcote, J. H. Miller, J. F. Diaz, K. H. Downing, E. Nogales, Insights into the Distinct Mechanisms of Action of Taxane and Non-Taxane Microtubule Stabilizers from Cryo-EM Structures. *J Mol Biol* **429**, 633-646 (2017).
53. P. Emsley, K. Cowtan, Coot: model-building tools for molecular graphics. *Acta Crystallogr D Biol Crystallogr* **60**, 2126-2132 (2004).
54. P. V. Afonine, B. K. Poon, R. J. Read, O. V. Sobolev, T. C. Terwilliger, A. Urzhumtsev, P. D. Adams, Real-space refinement in PHENIX for cryo-EM and crystallography. *Acta Crystallogr D Struct Biol* **74**, 531-544 (2018).
55. W. J. H. Hagen, W. Wan, J. A. G. Briggs, Implementation of a cryo-electron tomography tilt-scheme optimized for high resolution subtomogram averaging. *J Struct Biol* **197**, 191-198 (2017).
56. T. Grant, N. Grigorieff, Measuring the optimal exposure for single particle cryo-EM using a 2.6 A reconstruction of rotavirus VP6. *Elife* **4**, e06980 (2015).

57. A. Rohou, N. Grigorieff, CTFFIND4: Fast and accurate defocus estimation from electron micrographs. *J Struct Biol* **192**, 216-221 (2015).
58. B. Turonova, F. K. M. Schur, W. Wan, J. A. G. Briggs, Efficient 3D-CTF correction for cryo-electron tomography using NovaCTF improves subtomogram averaging resolution to 3.4A. *J Struct Biol* **199**, 187-195 (2017).
59. V. B. Chen, W. B. Arendall, 3rd, J. J. Headd, D. A. Keedy, R. M. Immormino, G. J. Kapral, L. W. Murray, J. S. Richardson, D. C. Richardson, MolProbity: all-atom structure validation for macromolecular crystallography. *Acta Crystallogr D Biol Crystallogr* **66**, 12-21 (2010).

Acknowledgments: We are very grateful to Patrick Meraldi and his colleagues (University of Geneva) for introducing us to the kinetic SiR-tubulin microtubule depolymerization assay. We acknowledge support from the University of Leicester Core Biotechnology Services (CBS) for DNA sequencing, construct preparation and confocal imaging, and Robert Markus at the School of Life Sciences Imaging Facility at the University of Nottingham for super-resolution microscopy. Single-particle cryo-EM data was collected with Rebecca Thompson at the Astbury Biostructure Laboratory, University of Leeds.

Funding: This work was funded by grants from Worldwide Cancer Research (16-0119) and The Wellcome Trust (204801/Z/16/Z) to A.M.F., the Medical Research Council, U.K. (MR/R000352/1) to C.A.M., Cancer Research UK (C24461/A23302) to R.B., and The Wellcome Trust (200870/Z/16/Z) and Lister Institute of Preventive Medicine to A.S. R.A. was supported by a PhD studentship from the Biotechnology and Biological Sciences Research Council, U.K. The FEI Titan Krios microscopes were funded by the University of Leeds (UoL ABSL award) and Wellcome Trust (108466/Z/15/Z). Cryo-electron tomography data were collected on a Polara microscope funded by grants from the Wellcome Trust (079605/Z/06/Z) and the BBSRC (BB/L014211/1).

AUTHOR CONTRIBUTIONS

RA, JM, JA, LO'R, AS, RB, CAM and AMF designed research; RA, JM, LO'R and DR performed research; RA, JM, LO'R and MR contributed new reagents; RA, JM, JA, LO'R, KS, DR, AS, RB and AMF analysed data; RA, JM, JA, LO'R, AS, RB, CAM and AMF wrote the paper.

COMPETING INTERESTS

The authors declare no conflict of interest.

Data and materials availability: Cryo-EM structures have been deposited as EMD-0331, PDB ID 6I2I.

FIGURE LEGENDS

Figure 1. EML4 exhibits reduced affinity for microtubules in mitosis

(**A**) Schematic representation of full-length human EML4 indicating the trimerisation (TD, pink), basic region (brown) and TAPE (blue) domains. Epitopes recognised by the two commercial EML4 antibodies (red) map to residue 150-200 (N-term Ab) and 951-981 (C-term Ab). (**B**) Lysates prepared from U2OS cells that were either mock-depleted or depleted of EML4 for 72 hours were analysed by Western blot with antibodies indicated. (**C & D**) U2OS cells were either mock-depleted or depleted of EML4 for 72 hours before being stained with the EML4 antibodies indicated (green) and α-tubulin (red) antibodies. Scale bars, 5 μm. Images are representative of three independent experiments. (**E & F**) U2OS cells were stained with the EML4 antibodies indicated (green) and α-tubulin (red) antibodies and imaged by confocal microscopy. Magnified views (zoom) are shown as merges. Scale bars, 5 μm. Images are representative of three independent experiments. (**G** & **H**) Co-localization between EML4 and microtubules for cells shown in (E and F) are shown with the y-axis indicating the mean Pearson's correlation coefficient (R) from 5 lines per cell in 10 cells per experiment showing means ± SD from three independent experiments. (**I**) U2OS cells were mock transfected or transfected with YFP-EML4 24 h before being stained with GFP and α-tubulin antibodies. DNA was stained with Hoechst 33258 (blue). Scale bars, 5 μm. (**J**) Co-localization between the GFP and microtubules for cells shown in I was calculated as in G and H. Data are means ± SD from 30 cells pooled from three independent experiments.

Figure 2. The EML4 NTD binds microtubules and is phosphorylated in mitosis

(**A**) HeLa and U2OS cells were either untreated (I, interphase) or treated with nocodazole for 16 hours to arrest them in mitosis (M) before being lysed and analysed via Western blot with antibodies indicated (pHH3, phospho-histone H3). (**B**) U2OS cells were transfected with the EML4 constructs indicated before being fixed and stained with antibodies against GFP (green), α-tubulin (red). DNA was stained with Hoeschst 33258 (blue). Scale bar, 5 μm. Images are representative of three independent experiments. (**C**) Co-localization between the GFP and microtubules for cells shown in B was calculated, with the y-axis indicating the mean Pearson's correlation coefficient (R) from 5 lines per cell in 10 cells per experiment showing means ± SD from three independent experiments. (**D**) U2OS cells were transfected with YFP alone or YFP-EML4-NTD for 24 hours before being treated and analysed by Western blot as in A. (**E**) U2OS cells were transfected with YFP-EML4-NTD for 24 hours before lysates were treated with λ-PPase (enzyme units indicated) for 30 mins and analysed by Western blot with antibodies indicated. Images are representative of three independent experiments. M. wts (kDa) are indicated in A, D & E.

Figure 3. NEK6 and NEK7 regulate association of EML4 with microtubules

(**A**) Schematic representation of full-length EML4 with TD and TAPE domains for reference, indicating the phosphorylation sites detected by mass spectrometry following incubation in vitro with NEK6 (blue) or NEK7 (green). Sites phosphorylated by both kinases are indicated in red. (**B**) Sequence alignment from species across the five vertebrate classes of the EML4 NTD region spanning the three identified phosphorylation sites (in red). (**C**) U2OS cells were transfected with YFP-EML4-NTD (wild-type, WT, and point mutants) for 24 hours before treating with nocodazole for 16 hours to arrest cells in mitosis. Cell lysates were analysed by Western blot with antibodies indicated. (**D**) U2OS cells were transfected with YFP-tagged full-length EML4 that was either WT or an S144/146A double mutant for 24 hours before being stained with GFP (green) and α-tubulin (red) antibodies. Merge images include DNA stained with Hoechst 33258 (blue). Scale bars, 5 μm. Images are representative of three independent experiments. (**E**) The mean Pearson's correlation coefficient for co-localization between EML4 and microtubules for cells shown in D was calculated from 5 lines per cell in 10 cells per experiment showing means ± SD from three independent experiments. (**F**) U2OS cells transfected with YFP-EML4-NTD were either mock-depleted or depleted of NEK6, NEK7 or NEK9 48 hours before being treated with nocodazole for 16 hours to arrest cells in mitosis. Cell lysates were analysed by Western blot with the antibodies indicated. (**G**) Untransfected U2OS cells were either mock-depleted or depleted of NEK6, NEK7 or NEK9 for 72 hours before being stained with EML4 (green) and α-tubulin (red) antibodies. DNA was stained with Hoechst 33258 (blue in merge). Scale bars, 5 μm. Images are representative of three independent experiments. (**H**) The mean Pearson's correlation coefficient for co-localization between EML4 and microtubules for cells shown in G was calculated from 5 lines per cell in 10 cells per experiment showing means ± SD from three independent experiments.

Fig. 4. Subtilisin treatment of microtubules leads to loss of association of EML4 and EML1 in vitro

(**A**) Microtubules purified from HeLa cells were either untreated or incubated with subtilisin before re-purification to remove the enzyme. These were then incubated with purified EML4-NTD before sedimentation to generate a supernatant (S) and pellet (P) fraction. Samples were then analysed by SDS-PAGE and Coomassie Blue stain. Data are means ± SD from three independent experiments. (**B & C**) The mean relative fraction of the EML4-NTD protein present in the pellet fraction represented in (A) is shown for two different concentrations of the EML4-NTD protein. Data are means ± SD from three independent experiments. (**D**) TIRF image of fluorescently labelled microtubules (left panel) treated with (purple) or without (green) subtilisin before incubation with YFP-EML1-NTD (residues 1-174) (right panel). Images are representative of three independent experiments. (**E**) Box plots reveal YFP intensity (a.u., arbitrary units) associated with untreated (561 nm) or subtilisin-treated (640

nm) microtubules. Boxes represent quartiles; whiskers show 10/90% data ± SD (n>200 microtubules).

Figure 5. Super-resolution and cryo-electron microscopy reveal EML4-NTD binding microtubules through a flexible interaction with α- and β-tubulin C-terminal tails

(**A**) U2OS cells were stained with EML4 (C-term Ab; magenta) and α-tubulin (green) antibodies and imaged by SIM. Arrowheads indicate examples of clusters of EML4 foci that co-localise with microtubules and are shown as magnified images in (b). Scale bar, 5 μm. Images are representative of three independent experiments. (**B**) Magnified views of endogenous EML4 bound to microtubules as taken from (A). (**C**) Section through a cryo-tomogram of an EML4 decorated microtubule. The microtubule lumen is indicated in light blue false colour. Red arrows indicate clear microtubule-bound densities, with sizes consistent with EML4-NTD trimers. Red arrowhead: in some regions, a periodicity of 4 nm for extra densities was observed, consistent with binding to both α- and β-tubulin. Scale bar, 30 nm. (**D**) 4.4 Å resolution C1 single-particle cryo-electron microscopy reconstruction of EML4-NTD decorated 13 protofilament microtubules, low pass filtered to 20 Å. Density within 9 Å of the fitted α- and β-tubulin atomic models is indicated with light and dark grey respectively; and defined, connected density >9Å away is indicated with red. (**E**) 3.6 Å resolution symmetrised reconstruction, showing two tubulin dimers within a single protofilament. Local resolution filtered α-tubulin and β-tubulin density is shown as transparent light and dark grey density respectively. The fitted H12 atomic model is shown as ribbons, with the flexible C-terminal tails indicated by dashed lines. The reconstruction low-pass filtered to 20 Å is also shown as mesh, with extra densities associated with α- and β-tubulin coloured in red and orange respectively.

Figure 6. Displacement of EML4 from microtubules reduces their stability in mitosis

(**A**) U2OS cells were either mock-depleted or depleted of EML4 with one of two siRNAs (siEML4.1 or siEML4.2) for 72 hours before being either left untreated or treated with 75 nM nocodazole for 2 hours. Cells were stained with α-tubulin antibodies. Scale bars, 5 μm. Images are representative of three independent experiments. (**B**) Microtubule sedimentation assay performed with lysates prepared from U2OS cells that were either mock- or EML4-depleted before Western blotting the pellet (P) and supernatant (S) fractions for α-tubulin. (**C**) Quantification of the % tubulin in the pellet fraction represented in (B). Data are means ± SD from three independent experiments. (**D**) Western blot analysis with antibodies indicated of lysates from U2OS cells that were either mock- or EML4-depleted. (**E & F**) Quantification of the acetylated or detyrosinated tubulin bands, respectively, after EML4 depletion relative to mock-depletion from blots represented in (D). Data are means ± SD from three independent experiments. (**G**) U2OS cells were transfected with YFP-EML4-WT or YFP-EML4-S144/146A,

incubated with SiR-Tubulin to visualise microtubules and SiR-Tubulin intensity measured every 60 s following addition of nocodazole. Stills from representative movies are shown with time since addition of nocodazole (min) indicated. Scale Bar, 5 μm. (**H**) The relative SiR-Tubulin intensity of cells in G is shown. Data represent means from 3 separate experiments with a minimum of 10 positions per condition.

Figure 7. A phosphonull EML4 mutant interferes with chromosome congression and activates the SAC

(**A**) HeLa:EGFP-LaminA/mCherry-H2B cells were either untransfected (left column) or transfected with YFP-EML4 wild-type protein (WT, middle column) or YFP-EML4-S144/146A (right column) for 24 hours before time-lapse confocal imaging. Stills from representative movies are shown with time (mins) indicated from mitotic entry. Scale bar, 7.5 μm. Images are representative of three independent experiments. (**B & C**) Quantification of cells from A indicating time from nuclear envelope breakdown (NEBD) to last chromosome congressed (left graph) and time from last chromosome congressed to anaphase onset (right graph). Data are means of cumulative frequencies ± SD; n=20. (**D**) U2OS cells were either untransfected or transfected with YFP-EML4-FL, EML4-WT or EML4-S144/146A, for 24 hours before being treated with RO-3306 for 16 hours, followed by 4 hours with MG132. Cells were then fixed and stained with GFP and α-tubulin antibodies. Merged images include DNA stained with Hoechst 33258 (blue). Scale bars, 5 μm. Images are representative of three independent experiments. (**E**) Quantification of the percentage of cells with normal or uncongressed chromosome in mitosis from at least 30 cells represented in (D). Data are means ± SD from 30 cells pooled from 3 independent experiments. (**F**) U2OS cells were either untransfected or transfected with EML4-S144/146A for 24 hours before being fixed and stained with antibodies against GFP (green) and BUBR1 (red). Merged images include DNA stained with Hoechst 33258 (blue). Scale bars, 5 μm. Images are representative of three independent experiments. (**G**) The relative intensity of BUBR1 was quantified and plotted relative to that in control samples. Data are means ± SD from 30 cells pooled from three independent experiments. (**H**) Histogram shows the mitotic index upon MPS1 inhibition (MPS1i) in U2OS cells transfected with either EML4-WT or -S144/146A constructs. Data are means ± SD from three independent experiments.

Figure 8. Phospho-dependent regulation of EML4 microtubule binding affinity

(**A**) Schematic model illustrating how the NEK9-NEK6-NEK7 kinases regulate affinity of EML4 for microtubules at the G2/M transition. Phosphorylation of two sites within the EML4 NTD as a result of activation of these kinases reduces electrostatic interaction of this basic region of EML4 for the acidic microtubule surface. (**B**) Cartoon showing electrostatic interaction of the basic NTD of the trimeric EML4 protein with the acidic tubulin C-terminal tails (green).

Table 1. Cryo-EM data collection, refinement and validation statistics

Data collection and processing information for the EML4-NTD bound 13-protofilament HeLa cell tubulin microtubule dataset, and refinement statistics for the HeLa cell tubulin dimer model asymmetric unit built into to the symmetrized electron density map.

*Microtubules exhibit pseudo-helical symmetry due to a symmetry break at the seam. 13-fold pseudo-helical symmetry was applied to the 13 protofilament microtubule reconstructions.

†The resolution value at the gold-standard Fourier Shell Correlation (FSC) 0.143 criterion between independently refined half-maps is shown for the central 15% of the reconstruction along the helical axis (isolated with a soft mask).

‡Average Fourier Shell Correlation (FCS) between the model and the symmetrized electron density map of the asymmetric unit (calculated around model atoms only).

§Root-mean-square (rms) deviations of bond lengths or angles in the model.

#As defined by the MolProbity validation server (*59*).

	(EMD-0331, PDB 6I2I)
Data collection and processing	
Pixel size (Å)	1.37Å
Symmetry imposed*	Pseudo-helical
Number of micrographs	1967
Initial particle images (no.)	44,946
Final particle images (no.)	19,542
Symmetrised Map resolution (Å) FSC threshold†	3.58Å Independent half-map FSC 0.143
Map resolution range (Å)	3.5-4.3Å
Refinement	
Initial models used	6DPU, 5SYF
Refinement resolution (Å) $FSC_{average}$‡	3.7 0.84
Map local sharpening *B*-factor ($Å^2$)	-90
Model composition Non-hydrogen atoms Protein residues Ligands	 41,058 5,256 18
rms deviations§ Bond lengths (Å) Bond angles (°)	 0.01 1.20
Validation# MolProbity score Clashscore Poor rotamers (%)	 1.91 8.24 0.5%
Ramachandran plot# Favored (%) Allowed (%) Outliers (%)	 92.73 7.27 0

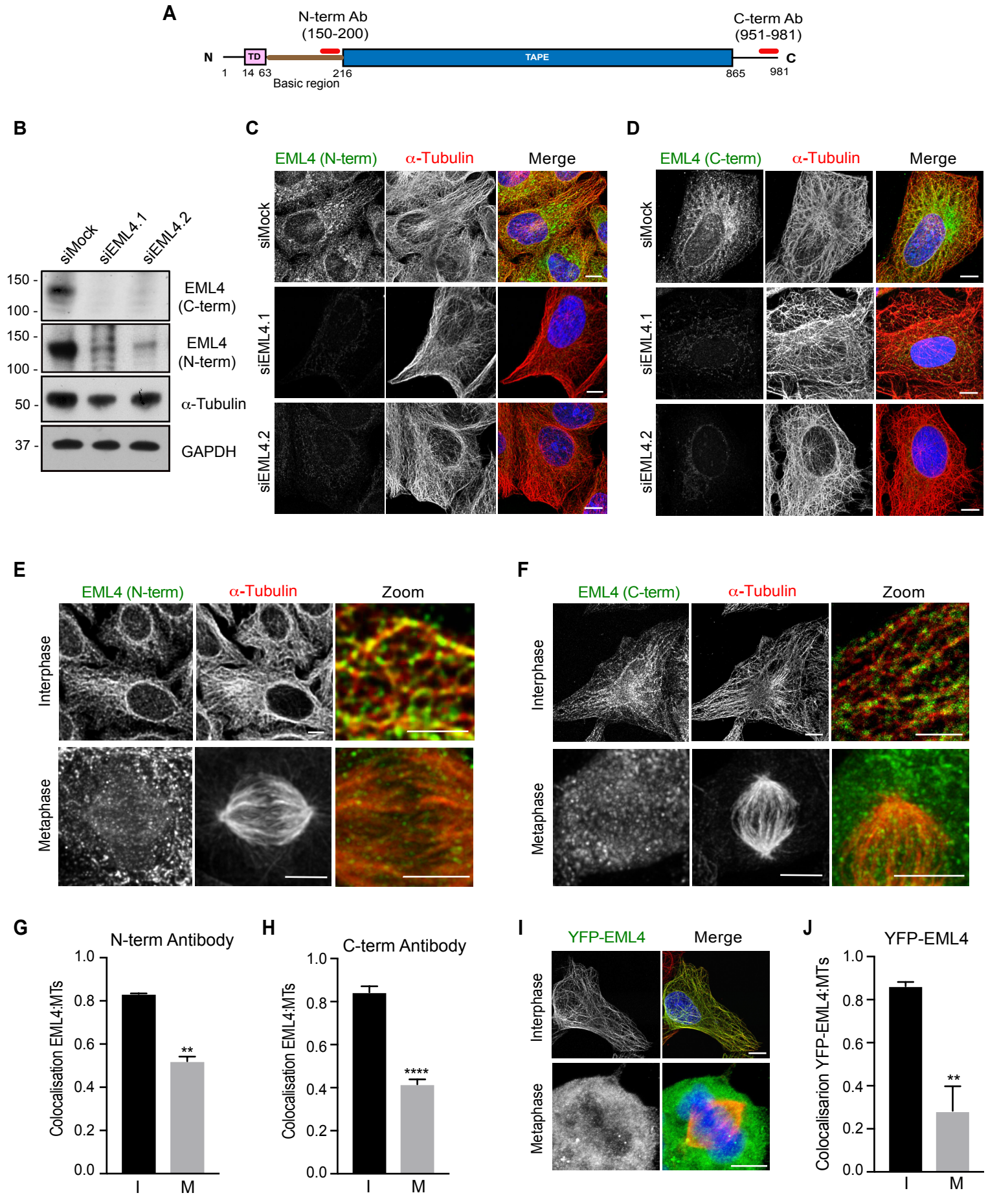
A
N-term Ab
(150-200)
C-term Ab
(951-981)
N
TD
TAPE
C
1
14
63
216
Basic region
865
981
B
siMock
siEML4.1
siEML4.2
150 -
100 -
150 -
100 -
50 -
37 -
EML4
(C-term)
EML4
(N-term)
α-Tubulin
GAPDH
C
EML4 (N-term)
α-Tubulin
Merge
siMock
siEML4.1
siEML4.2
D
EML4 (C-term)
α-Tubulin
Merge
siMock
siEML4.1
siEML4.2
E
EML4 (N-term)
α-Tubulin
Zoom
Interphase
Metaphase
F
EML4 (C-term)
α-Tubulin
Zoom
Interphase
Metaphase
G
N-term Antibody
Colocalisation EML4:MTs
1.0
0.8
0.6
0.4
0.2
0.0
**
I
M
H
C-term Antibody
Colocalisation EML4:MTs
1.0
0.8
0.6
0.4
0.2
0.0
****
I
M
I
YFP-EML4
Merge
Interphase
Metaphase
J
YFP-EML4
Colocalisarion YFP-EML4:MTs
1.0
0.8
0.6
0.4
0.2
0.0
**
I
M

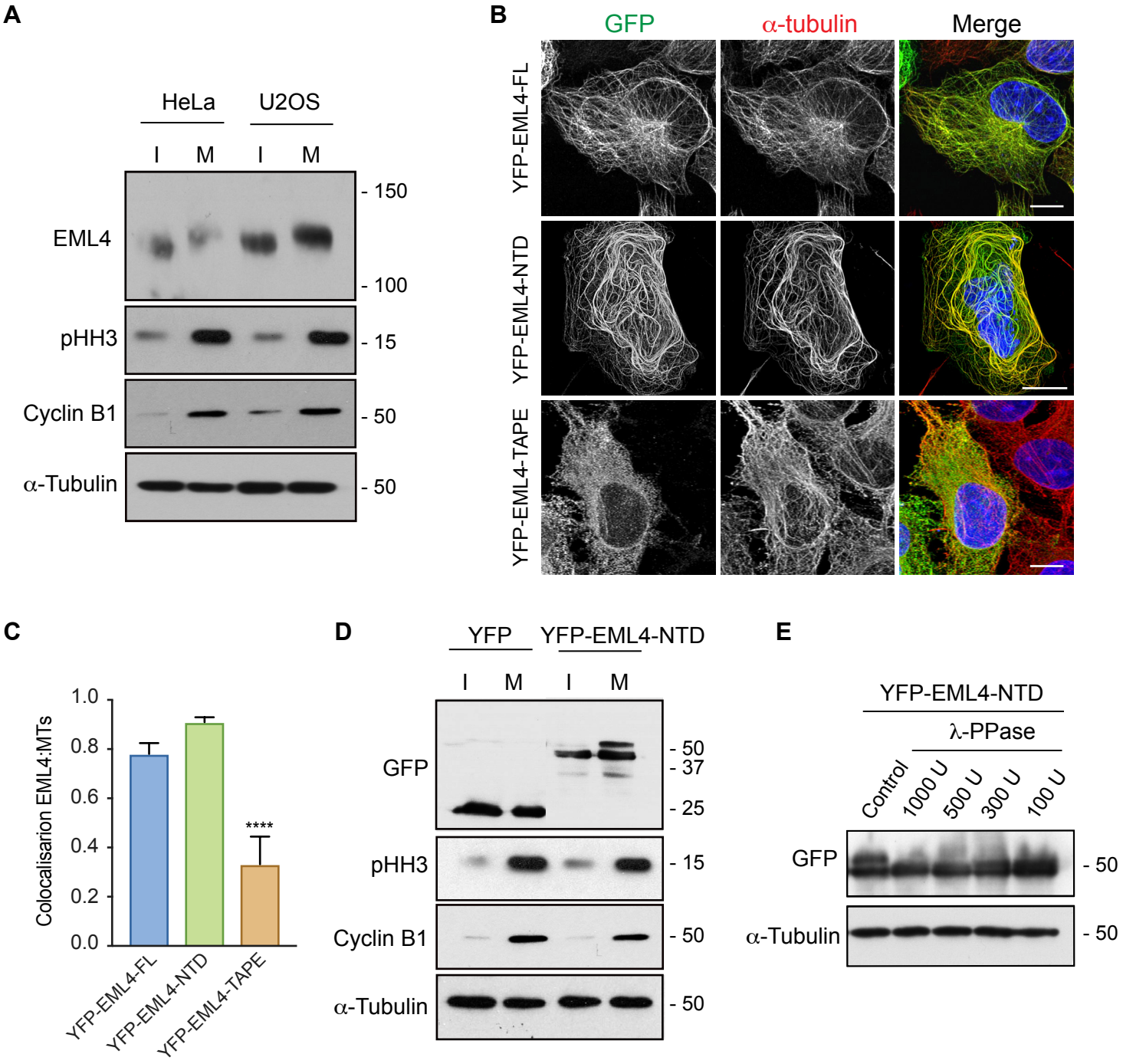
A
HeLa
U2OS
I
M
I
M
EML4
pHH3
Cyclin B1
α-Tubulin
- 150
- 100
- 15
- 50
- 50
B
GFP
α-tubulin
Merge
YFP-EML4-FL
YFP-EML4-NTD
YFP-EML4-TAPE
C
Colocalisarion EML4:MTs
1.0
0.8
0.6
0.4
0.2
0.0
****
YFP-EML4-FL
YFP-EML4-NTD
YFP-EML4-TAPE
D
YFP
YFP-EML4-NTD
I
M
I
M
GFP
pHH3
Cyclin B1
α-Tubulin
- 50
- 37
- 25
- 15
- 50
- 50
E
YFP-EML4-NTD
λ-PPase
Control
1000 U
500 U
300 U
100 U
GFP
α-Tubulin
- 50
- 50

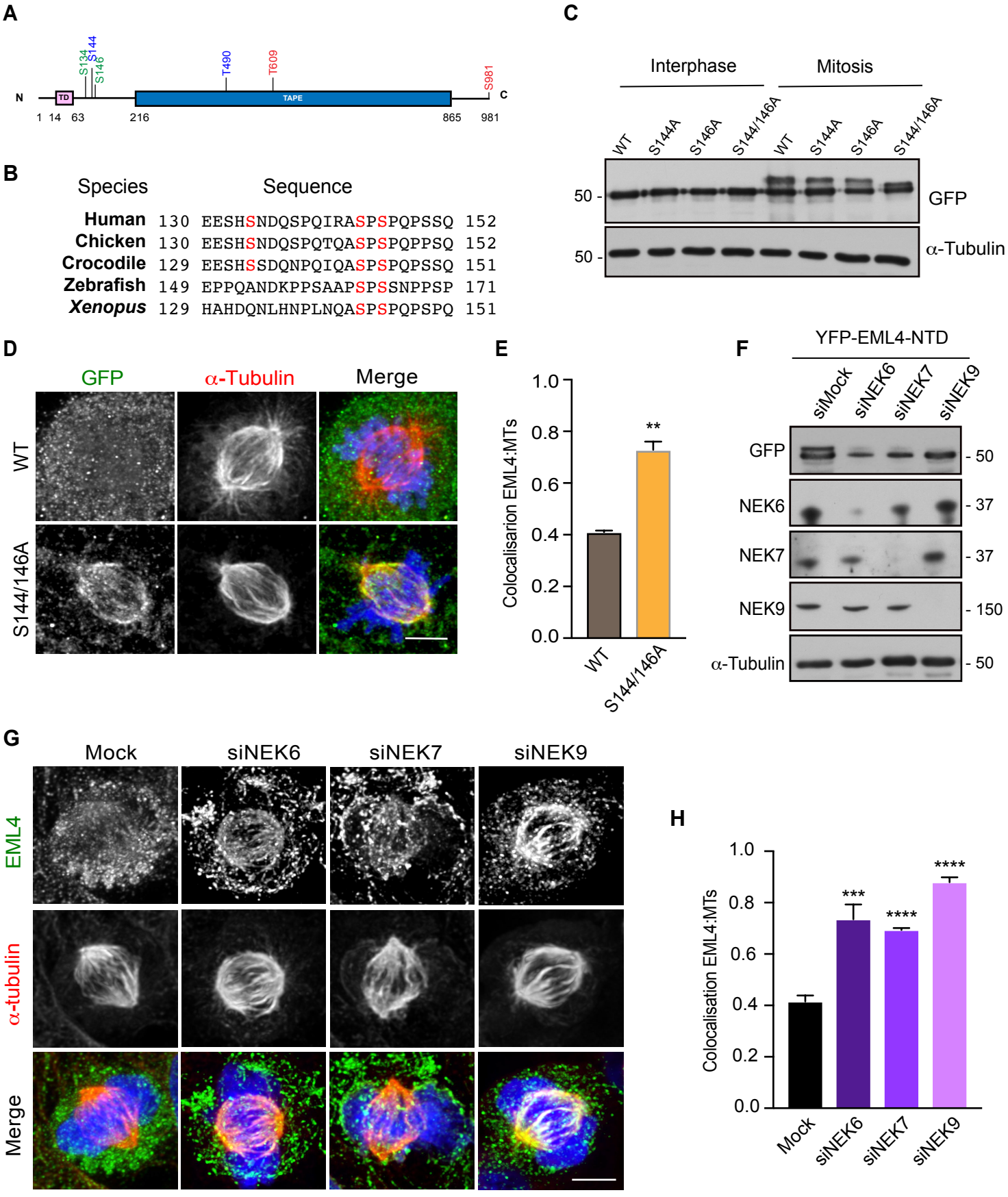
A
S134
S144
S146
T490
T609
S981
N
TD
TAPE
C
1 14 63 216 865 981
B
Species Sequence
Human 130 EESHSNDQSPQIRASPSPQPSSQ 152
Chicken 130 EESHSNDQSPQTQASPSPQPPSQ 152
Crocodile 129 EESHSSDQNPQIQASPSPQPSSQ 151
Zebrafish 149 EPPQANDKPPSAAPSPSSNPPSP 171
Xenopus 129 HAHDQNLHNPLNQASPSPQPSPQ 151
C
Interphase
Mitosis
WT
S144A
S146A
S144/146A
50 -
GFP
α-Tubulin
D
GFP
α-Tubulin
Merge
WT
S144/146A
E
Colocalisarion EML4:MTs
1.0
0.8
0.6
0.4
0.2
0.0
**
WT
S144/146A
F
YFP-EML4-NTD
siMock
siNEK6
siNEK7
siNEK9
GFP
NEK6
NEK7
NEK9
α-Tubulin
- 50
- 37
- 37
- 150
- 50
G
Mock
siNEK6
siNEK7
siNEK9
EML4
α-tubulin
Merge
H
Colocalisation EML4:MTs
1.0
0.8
0.6
0.4
0.2
0.0
***
****
****
Mock
siNEK6
siNEK7
siNEK9

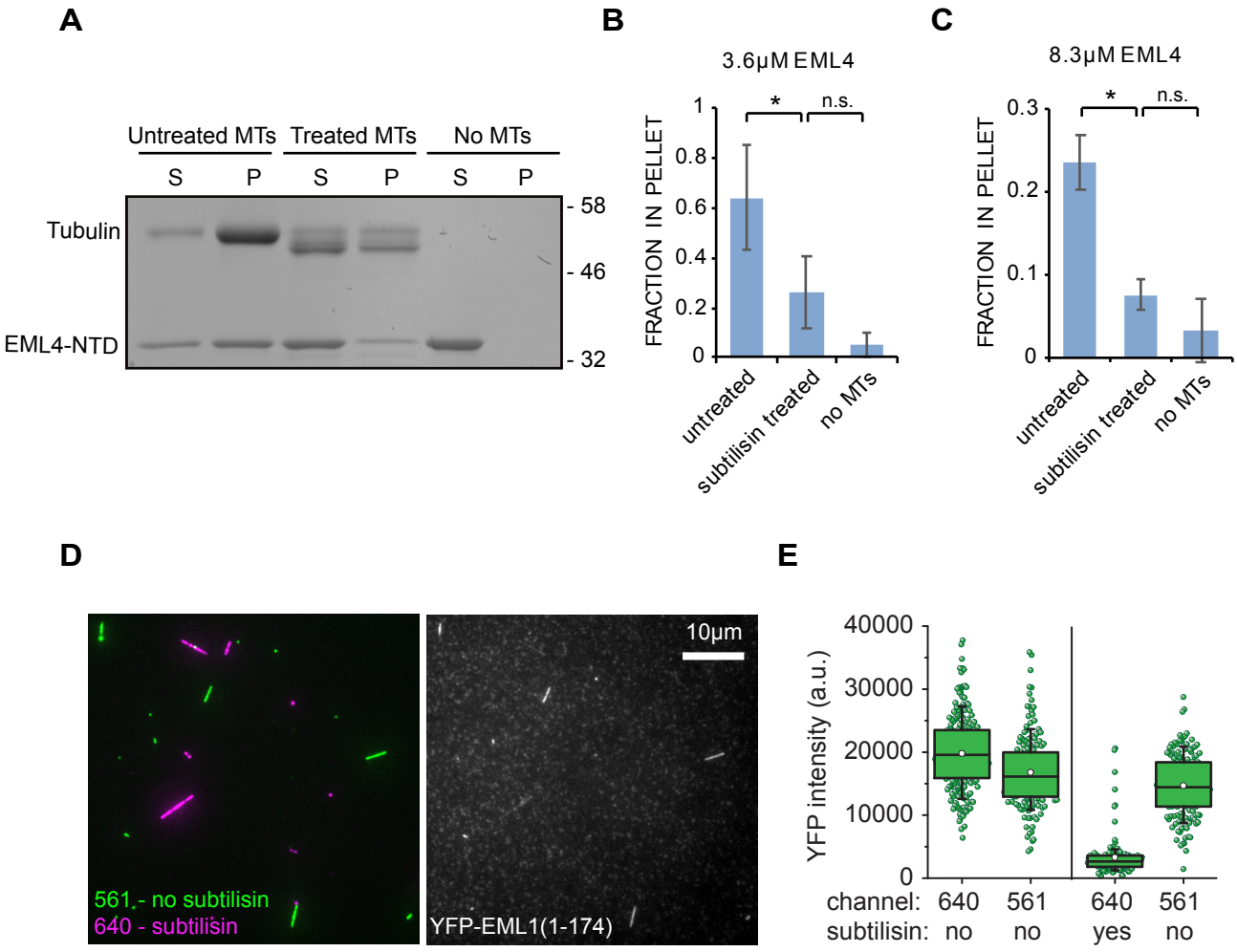
A
Untreated MTs
Treated MTs
No MTs
S
P
S
P
S
P
Tubulin
EML4-NTD
- 58
- 46
- 32
B
3.6μM EML4
FRACTION IN PELLET
1
0.8
0.6
0.4
0.2
0
*
n.s.
untreated
subtilisin treated
no MTs
C
8.3μM EML4
FRACTION IN PELLET
0.3
0.2
0.1
0
*
n.s.
untreated
subtilisin treated
no MTs
D
561,- no subtilisin
640 - subtilisin
10μm
YFP-EML1(1-174)
E
YFP intensity (a.u.)
40000
30000
20000
10000
0
channel: 640 561 640 561
subtilisin: no no yes no

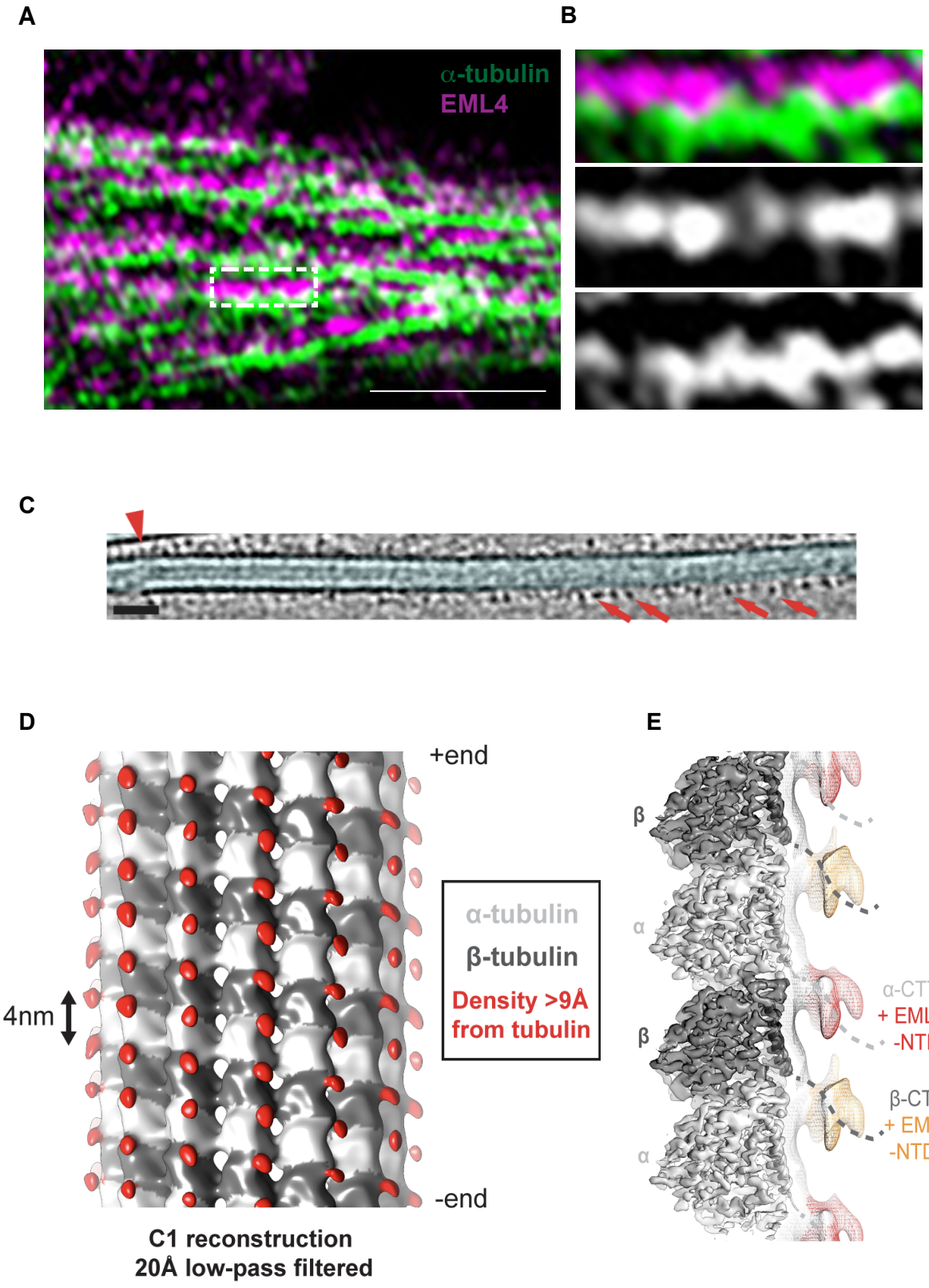
A
α-tubulin
EML4
B
C
D
+end
4nm
α-tubulin
β-tubulin
Density >9Å
from tubulin
-end
C1 reconstruction
20Å low-pass filtered
E
β
α
β
α
α-CTT
+ EML4
-NTD
β-CTT
+ EML4
-NTD

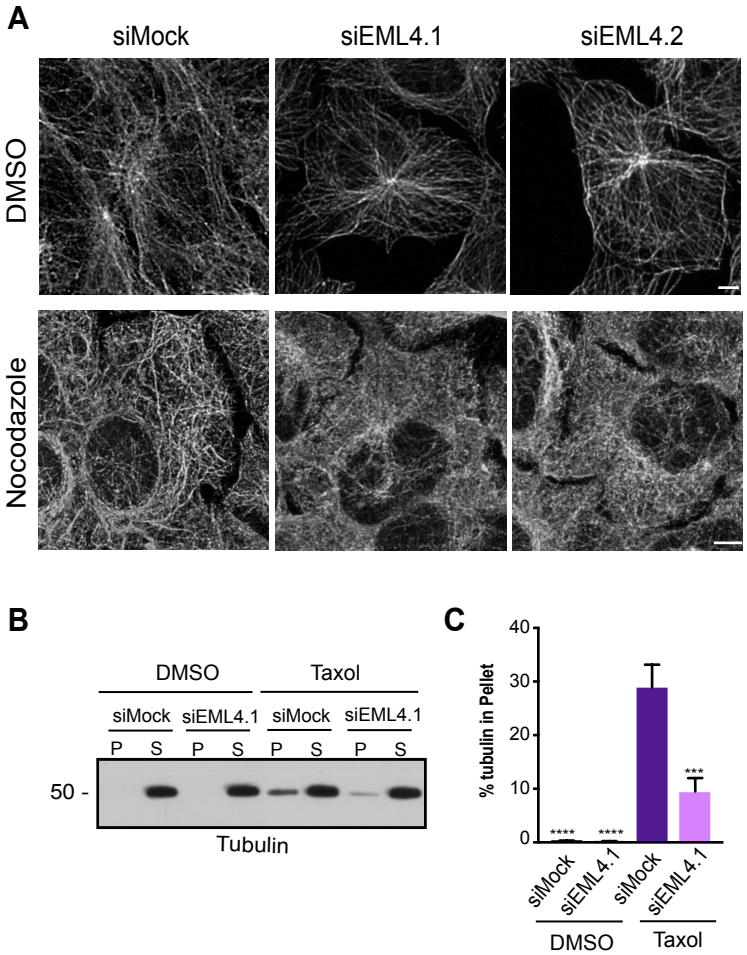
A
siMock
siEML4.1
siEML4.2
DMSO
Nocodazole
B
DMSO
Taxol
siMock
siEML4.1
siMock
siEML4.1
P S P S P S P S
50 -
Tubulin
C
% tubulin in Pellet
40
30
20
10
0
****
****
***
siMock
siEML4.1
siMock
siEML4.1
DMSO
Taxol
D
siMock
siEML4.1
siEML4.2
150 -
100 -
50 -
50 -
50 -
37 -
EML4
Ac. Tub
Detyro. Tub
Tubulin
GAPDH
E
Ac. Tub
Relative intensity
1.0
0.5
0.0
***
****
siMock
siEML4.1
siEML4.2
F
Detyro. Tub
Relative intensity
1.0
0.5
0.0
***
***
siMock
siEML4.1
siEML4.2
G
WT
S144/146A
0
0
7
7
14
14
H
YFP-EML4-WT
YFP-EML4-S144/146A
Relative siR-tubuln Intensity
1.2
1.0
0.8
0.6
0.4
0.2
0.0
p = 0.0274
0 1 2 3 4 5 6 7 8 9 10 11 12 13 14
Time since addition of nocodazole (min)

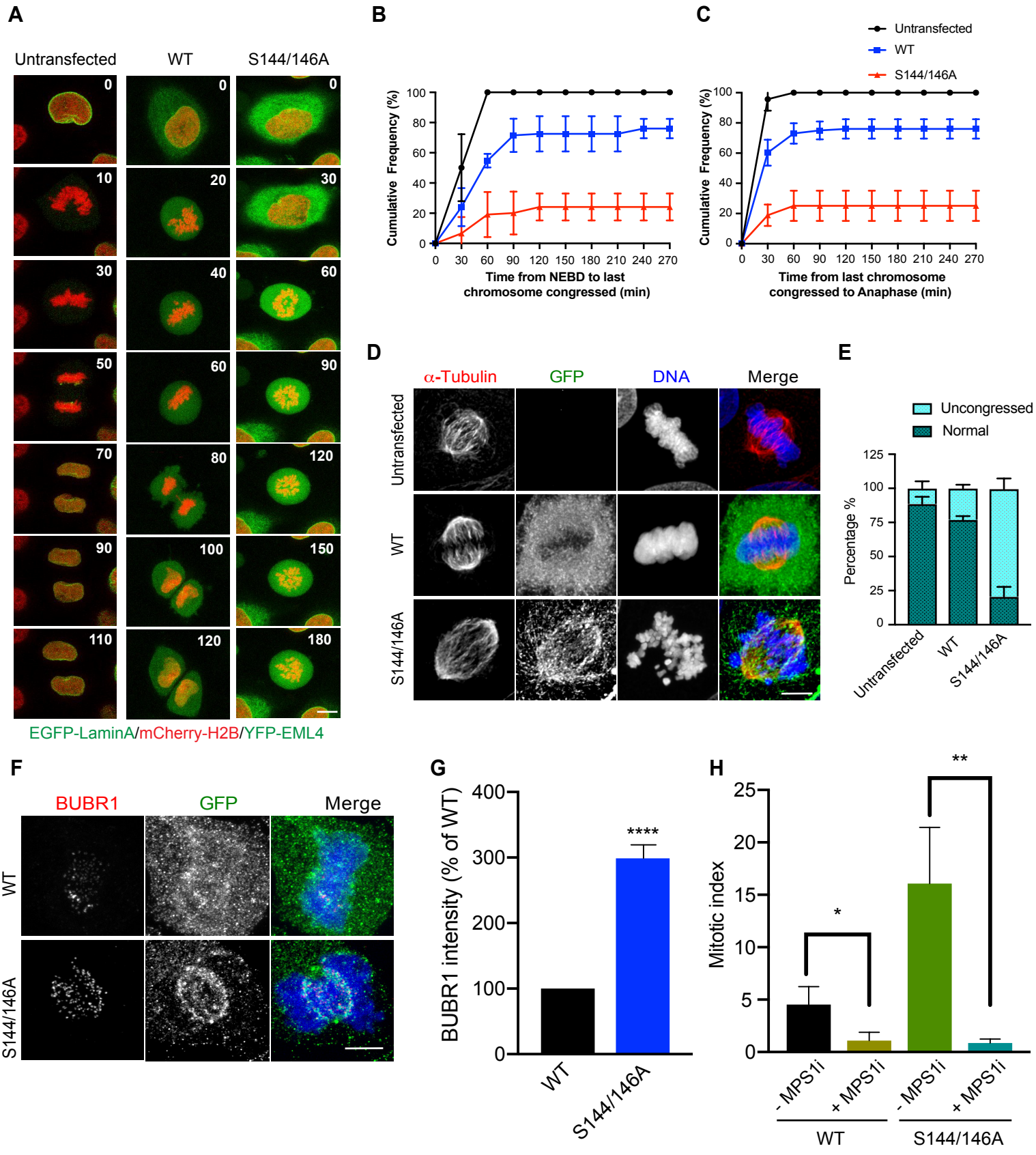
A
Untransfected
WT
S144/146A
EGFP-LaminA/mCherry-H2B/YFP-EML4
B
Cumulative Frequency (%)
Time from NEBD to last chromosome congressed (min)
C
Untransfected
WT
S144/146A
Cumulative Frequency (%)
Time from last chromosome congressed to Anaphase (min)
D
α-Tubulin
GFP
DNA
Merge
Untransfected
WT
S144/146A
E
Uncongressed
Normal
Percentage %
Untransfected
WT
S144/146A
F
BUBR1
GFP
Merge
WT
S144/146A
G
BUBR1 intensity (% of WT)
****
WT
S144/146A
H
Mitotic index
*
**
- MPS1i
+ MPS1i
- MPS1i
+ MPS1i
WT
S144/146A

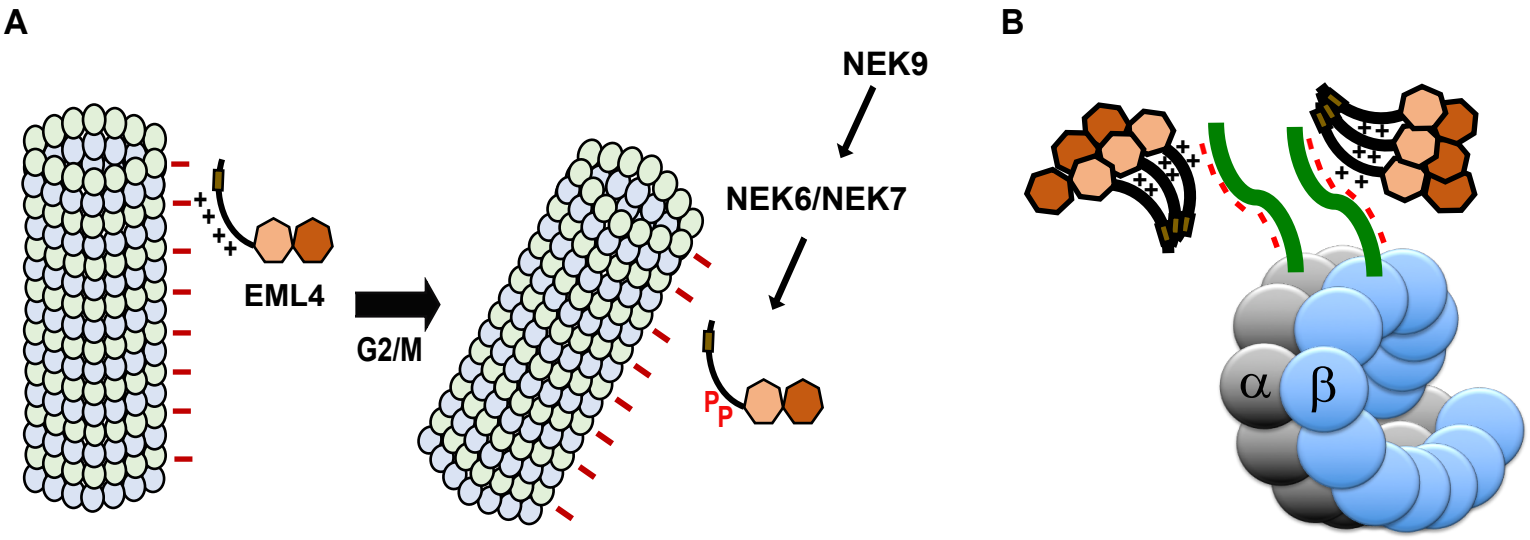
A
NEK9
NEK6/NEK7
EML4
G2/M
P
P
B
α
β

SUPPLEMENTARY INFORMATION

Adib et al. Figure S1

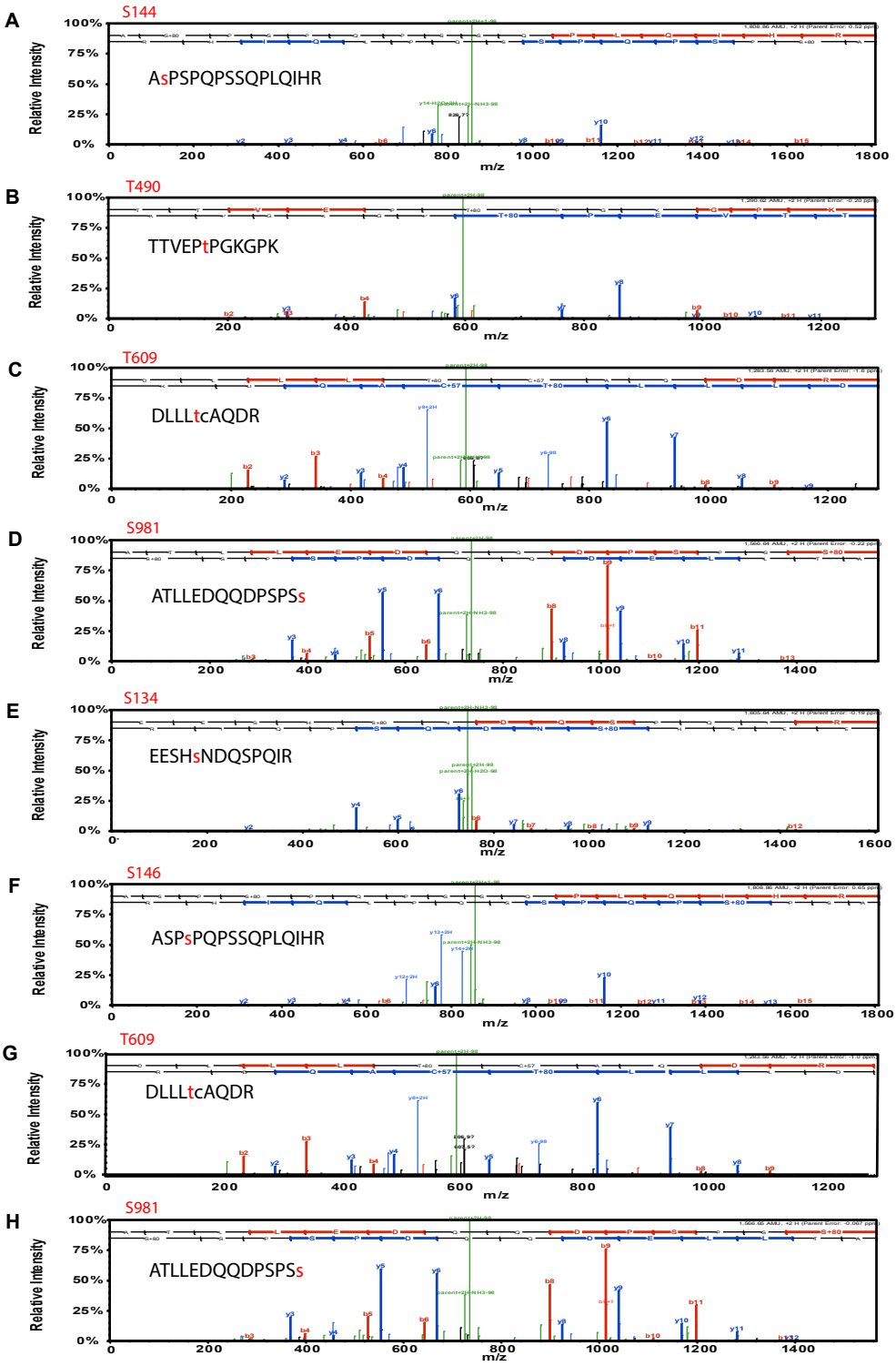

Supplementary Figure S1. Mass spectrometry profiles of EML4 phosphorylation sites

Purified EML4 protein was phosphorylated with NEK6 and NEK7 in vitro. Mass spectrometry profiles are presented of peptides isolated following incubation with NEK6 (A-D) or NEK7 (E-H). Phosphorylated amino acids are indicated in red in the identified peptide.

Adib et al. Figure S2

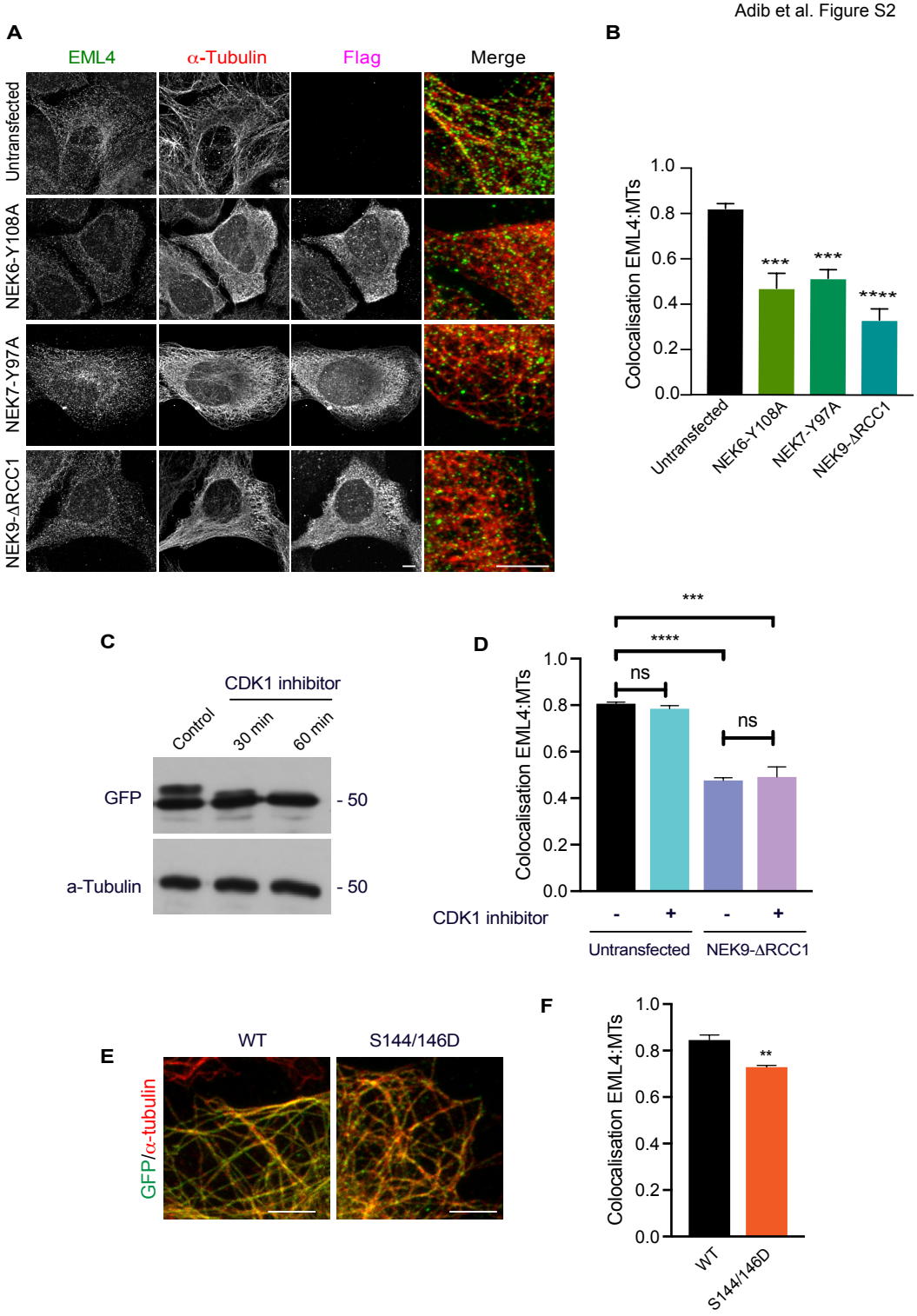

Supplementary Figure S2. Activated NEK6, NEK7 and NEK9 reduce association of EML4 with interphase microtubules

(**A**) U2OS cells were transfected with YFP-tagged full-length EML4 that was either wild-type (WT) or an S144/146D double mutant for 24 hours before being stained with GFP (green) and α-tubulin (red) antibodies. Scale bars, 5 μm. Images are representative of three independent experiments. (**B**) The mean Pearson's correlation coefficient for co-localization between EML4 and microtubules for cells shown in A was calculated from 5 lines per cell in 10 cells; data are means ± SD from 30 cells pooled from 3 independent experiments. (**C**) U2OS cells were transfected with YFP-EML4-NTD for 24 hours before being treated with nocodazole for 16 hours to arrest cells in mitosis followed by treatment with the CDK1 inhibitor, RO-3306, for 0 (control), 30 or 60 min. Cell lysates were analysed by Western blot with the antibodies indicated. (**D**) U2OS cells were mock-transfected or transfected with Flag-NEK6-Y108A, Flag-NEK7-Y97A, or Flag-NEK9-ΔRCC1 for 24 hours before being stained with EML4, α-tubulin and Flag antibodies. Images are representative of three independent experiments. (**E**) The mean Pearson's correlation coefficient for co-localization between EML4 and microtubules was calculated from 5 lines per cell in 10 cells. Data are means ± SD from 30 cells pooled from 3 independent experiments. (**F**) U2OS cells were untransfected or transfected with Flag-NEK9-ΔRCC1 for 24 hours before being treated with or without the CDK1 inhibitor, RO-3306, as indicated. The mean Pearson's correlation coefficient for co-localization between EML4 and microtubules was calculated from 5 lines per cell in 10 cells per experiment showing means ± SD from 3 independent experiments.

Adib et al. Figure S3

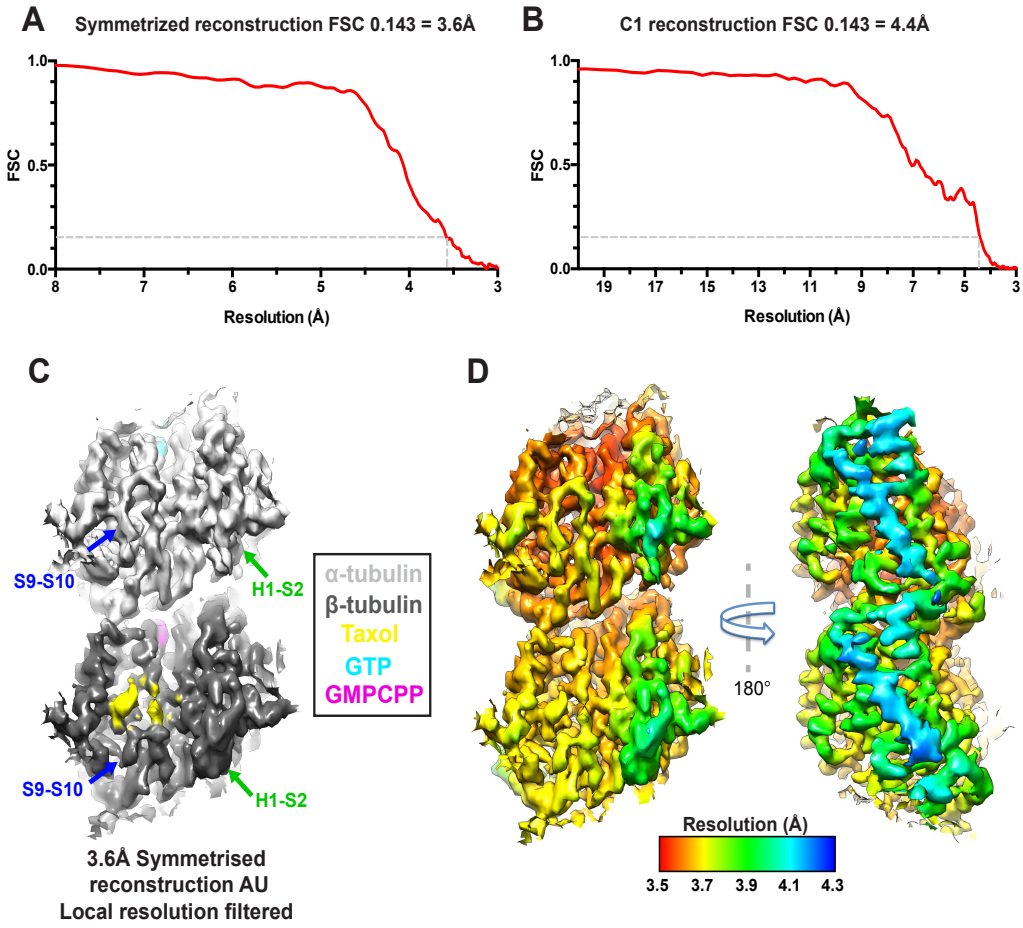

Supplementary Figure S3. Cryo-electron microscopy diagnostics and resolution estimation

(**A**) Gold-standard Fourier Shell Correlation (FSC) curve for the symmetrized 13 protofilament EML4-microtubule reconstruction. (**B**) Gold-standard FSC curve for the C1 13 protofilament EML4-microtubule reconstruction. The central 15% of the microtubule along the helical axis was isolated from the independently refined half-maps (using a soft-mask) for FSC

calculations. (**C**) An asymmetric unit in the symmetrized reconstruction viewed from the microtubule lumen, showing α- and β-tubulin in light and dark grey, respectively. Densities for GTP, GMPCPP and paclitaxel (included in the tubulin purification protocol) are indicated in cyan, magenta and yellow, respectively. Density for the S9-S10 and H1-S2 loops exhibit expected differences in α- and β-tubulin, indicating successful seam determination during the image alignment. Because of the reference used for alignment, the central, best region of the reconstruction spans across an inter-dimer longitudinal contact encompassing α- and β-tubulin from separate dimers. (**D**) Local resolution calculated in Relion for an asymmetric unit of the symmetrized reconstruction, showing lumenal (left) and outer (right) faces. A B-factor of -90 was applied to sharpen the reconstructions shown in panels C and D, up to local resolution cut-offs as displayed in panel D.

Adib et al. Figure S4

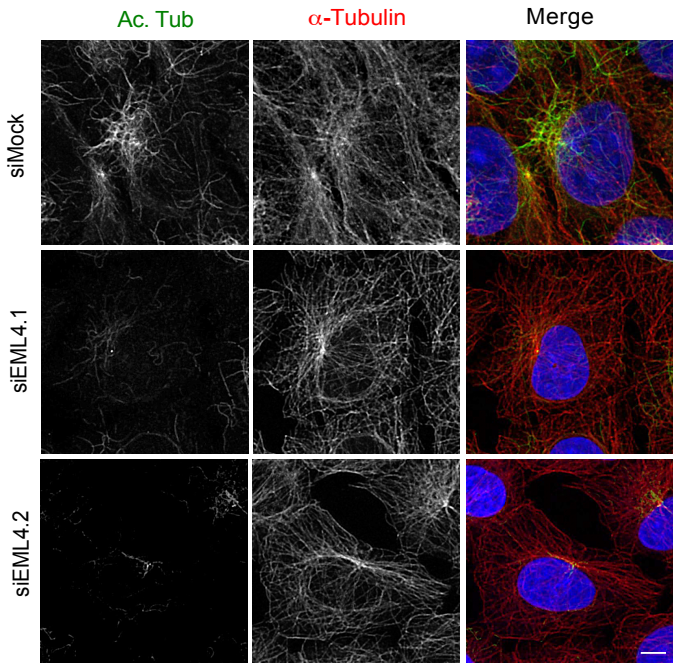

Supplementary Figure S4. EML4 depletion leads to reduced microtubule acetylation

U2OS cells were either mock or EML4-depleted for 72 hours before staining with acetylated tubulin (green) and α-tubulin (red) antibodies. Merge images include DNA stained with Hoechst 33258 (blue). Scale bar, 5 μm. Images are representative of three independent experiments.